International Journal of Heat and Mass Transfer 222 (2024) 125170

Contents lists available at ScienceDirect

International Journal of Heat and Mass Transfer

journal homepage: www.elsevier.com/locate/ijhmt

Effects of different cross-sections of Body Centered Cubic cells on pressure drop and heat transfer of additively manufactured heat sinks

Andrea Lorenzon, Emanuele Vaglio, Luca Casarsa *, Giovanni Totis

Polytechnic Department of Engineering and Architecture, University of Udine, Udine IT 33100, Italy

ARTICLE INFO

Keywords:
Laser Powder Bed Fusion
Heat sinks
Body centred cubic arrays
Heat transfer
Pressure losses

ABSTRACT

In many industrial applications, heat loads management requires the design and production of compact heat exchangers which are expected to handle high thermal loads with acceptable pressure losses, while assuring good mechanical performances. These challenging targets can be achieved by filling the cavities where the cool/hot fluid circulates with lattice structures promoting the heat exchange between the fluid and the cavity boundaries. Such lattice structures can be only produced through Additive Manufacturing due to their high geometric complexity. Recent experimental investigations proved the effectiveness of some kinds of lattice structures having a circular cross section. Here the aerothermal behaviour of Body-Centred Cubic (BCC) lattice stagger arrays in a rectangular channel was experimentally investigated by considerably extending the previous studies to higher Reynolds numbers (up to 30′000) and to new types of lattice structures. Specifically, three new BCC structures having a cam-like, drop-like and elliptical cross section were explored in this work and compared against those having circular cross section. All the samples were manufactured by means of Laser Powder Bed Fusion and made from AlSi10Mg. At first, the heat exchangers were comprehensively characterized by means of optical non-destructive methods. Successively they were tested in a dedicated rig by imposing constant heat flux boundary conditions. The characteristics of the transitional or fully turbulent approaching flow to the test section are also reported thanks to dedicated flow field measurements performed by Particle Image Velocimetry. According to the obtained results, the BCC structure with the circular cross section of larger diameter is the most effective in terms of heat transfer, although it is largely penalized by the pressure losses. Similar heat transfer performances were achieved by the tapered cross section of elliptical shape with the advantage of a considerably lower friction factor. Pressure losses resulted almost identical for all the tapered cross sections but lower than those of the circular one having an equal frontal dimension. When considering the thermal performance factor the circular shape becomes unfavourable for Re>20′000, while the elliptical cross section is the best choice to efficiently promote heat transfer up to Re=30′000.

1. Introduction

In the last years the increasing diffusion of Additive Manufacturing (AM) has enabled the use of Lattice Frame Materials (LFM) for producing compact heat exchangers for many engineering applications. LFMs consist of struts arranged to form an elementary structure that can be used to build up periodical reticular frames. These frames can be used as a single or multilayer core between confinement plates through which a cooling medium flows. Most common unit cell types employed in heat transfer applications are the Face Centered Cubic (FCC), the Body Centered Cubic (BCC), the pyramidal structure, the Kagome, or the more complicated configurations that can be generated by a larger number of ligaments such as the Kelvin and the Octet unit cells [1]. When arranged in a single layer, such structures may provide from 2 to 4 times the heat transfer rate of a smooth, empty channel, with the disadvantage of increasing the pressure drops of one order of magnitude [2–6]. However, the resulting Thermal Performance Factor (TPF) typically exceeds unity at least for low Reynolds numbers, indicating a high aero-thermal efficiency [7].

It has to be mentioned that AM obviously enables the production of much more complicated structures, such as Gyroids [8] or triple periodic types [9]. Despite the drawback of higher pressure losses in comparison with LFM geometries, they are preferred when a higher mechanical strength is required. However, similar results can be obtained by also adopting graded LFMs, as shown in [10]. From the industrial

* Corresponding author.
E-mail address: luca.casarsa@uniud.it (L. Casarsa).

https://doi.org/10.1016/j.ijheatmasstransfer.2024.125170
Received 15 June 2023; Received in revised form 5 December 2023; Accepted 1 January 2024
Available online 5 January 2024

Nomenclature

Latin symbols

a	struts major axis [m]
A_c	flow cross-section area [m^2]
A_r	reference surface area for heat transfer [m^2]
A_w	wetted surface area [m^2]
c_p	specific heat capacity [J/(kgK)]
d	struts minor axis [m]
D_{BCC}	hydraulic diameter of the heat sink [m]
D_h	hydraulic diameter [m]
E	supplied voltage [V]
f	friction factor
f_0	friction factor of the smooth channel
f^*	modified friction factor
h	heat transfer coefficient [W/m^2K]
$h_{0,IN}, h_{0,OUT}$	air total enthalpy at the inlet and outlet of the test section [J/kg]
H	channel height [m]
I	supplied current intensity [A]
k	thermal conductivity [W/(Km)]
L	entry channel length [m]ΔL
$\dot{m}$	distance between pressure taps [m]
air	flow rate [kg/s]
Nu	Nusselt number
Nu_0	Nusselt number of the smooth channel
Nu^*	modified Nusselt number
P	wet perimeter of the flow area [m]
Pr	Prandtl number
Δp	pressure drop [Pa]
Q_{air}	heat rate received by air [W]
Q_{el}	input heat power [W]
r	fillet radius [m]
R	overall thermal resistance [K/W]
Ra	roughness average [μm]
Re	channel Reynolds number
Re^*	modified channel Reynolds number
Re_{DNS}	Reynolds number of the DNS data
Rec	thermocouple recovery factor
S_x	streamwise pin spacing [m]
S_y	spanwise pin spacing [m]
T	air static temperature [°C]
T_{Al}	internal temperature of the instrumented aluminium block [°C]
T_{IN}	inlet air temperature [°C]
T_{OUT}	outlet air temperature [°C]
$T_{OUT,c}$	air temperature at the throat section [°C]
T_{read}	temperature value read by the thermocouple [°C]
T_w	internal channel surface temperature [°C]
TPF	thermal performance factor
ΔT_{ml}	log mean temperature difference [°C]
U	streamwise velocity [m/s]
U'	streamwise velocity fluctuation [m/s]
U_b	bulk velocity [m/s]
V_w	enclosed wetted volume [m^3]
W'	crosswise velocity fluctuations [m/s]
Wa	waviness average [μm]
X, Y, Z	channel reference system: streamwise, spanwise and crosswise directions

Greek symbols

ε	mean height of roughness [μm]
λ_c	cut-off wavelength [mm]
$\lambda_{c,FALG}$	cut-off wavelength of the linear areal Gaussian filter [mm]
μ	dynamic viscosity [Pa s]
ρ	density [kg/m^3]

Acronyms

AM	Additive Manufacturing
BCC	Body-Centered Cubic
CT	Computed Tomography
DNS	Direct Numerical Simulation
FFF	Fused Filament Fabrication
LFM	Lattice Frame Materials
LPBF	Laser Powder Bed Fusion
MDF	Medium-Density Fibreboard
FCC	Face Centered Cubic
PIV	Particle Image Velocimetry
SEM	Scanning Electron Microscope
SLA	Stereolithography
TC	Thermocouples
TPS	Transient Plane Source
XRD	X-ray diffraction

perspective, the selection of the most appropriate structure and its optimization is crucial for meeting the desired performance while containing the production time and cost [11].

Focusing on LFMs, the existing literature is extensive and covers a broad range of configurations that have been studied using multiple approaches (experimental or numerical) and under different operating conditions (e.g. Reynolds number range and thermal boundary conditions). Recently, a very good review was conducted on this topic by Caket et al. [12]. The authors analyzed and commented more than 100 papers focused on 3D LFM used for heat transfer enhancement and concluded that the most studied structures are the simple cubic, the Kagome, and the tetrahedral or octet lattice structures made from aluminum, copper or stainless steels and arranged in a single or multi-layer configuration. Most importantly, the authors pointed out that the majority of the investigations were carried out at Reynolds numbers below the approximate threshold of 20′000, thus limiting the possibilty of using the previous findings for advanced applications requiring high Reynolds numbers, such as in steel production [13], chemical processing [14], power generation plants [15] and internal cooling of gas turbine blades [16].

Moreover, it is woth recalling that different definitions of fundamental characteristic parameters describing the application (such as the characteristic length and the reference temperature) are generally adopted in literature, thus hindering a direct comparison between the obtained findings. This issue is exacerbated by the absence of a rigorous and standardized method for comprehensively characterizing the tested specimens from the morphological and surface quality point of view. This step is important because the actual structure shape and surface roughness affect the flow development and its pressure losses, with a direct impact on the final TPF.

Accordingly, the literature was thoroughly examined with the aim of providing an up-to-date overview on these topics. The analysis revealed that a large number of research works were based on pure numerical simulation by completely neglecting manufacturability issues and the real properties of the investigated structures. By limiting the analysis to the experimental studies on ordered lattice structures (excluding foams) produced through AM, a total of 25 articles were selected (Table 1). This group includes all the pertinent works discussed in [12] plus many other recent works of great relevance. Among these articles, 15 do not provide any geometric, morphological, or surface characterization of the

Table 1
Summary of the most relevant research works discussing real properties of advanced structures for heat management.

Ref.	Year	Structures	Production process	Experimental characterization
[17]	2014	Plate fins and flat	LPBF	Surface morphology, roughness (Optical scanner); surface morphology, porosity (Field Emission SEM); roughness (roughness tester); surface emissivity (infrared camera).
[18]	2017	Reticular	Polyjet, binder jetting	–
[19]	2018	Honeycomb	LPBF	Thermal conductivity (n.d.).
[20]	2018	Plate fins and reticular	LPBF	Unit cell size and truss defects (optical microscopy); roughness (light interferometer).
[21]	2018	Reticular	LPBF	Density (Archimedes principle), truss defects, truss geometry, surface morphology (optical microscope); roughness, surface morphology (confocal profiler); wettability (n.d.).
[22]	2019	Reticular	LPBF	–
[23]	2019	Reticular	metal 3D printing (not better specified)	–
[24]	2019	Reticular	LPBF	Thermal conductivity (temperature gradient method).
[25]	2019	Reticular	metal 3D printing (not better specified)	–
[26]	2019	Reticular	LPBF	–
[27]	2020	Microchannels, shaped bumps	LPBF	–
[28]	2020	Reticular	Binder Jetting	Roughness (roughness tester); geometry (n. d.).
[6]	2020	Reticular	SLA	–
[29]	2020	Reticular	LPBF	–
[30]	2021	Reticular	Binder Jetting	Geometry (nominal accuracy of the process).
[31]	2021	Reticular	SLA	–
[32]	2021	Radial heat sink	LPBF	–
[33]	2022	plane and slotted plate fins	FFF+Digital Metal Casting	–
[34]	2022	Reticular	LPBF	–
[35]	2022	Reticular	Polymer Additive Manufacturing (not specified)	–
[36]	2023	integral fins, reticular	SLA	–
[37]	2023	Microchannels	3D printed scaffold-removal	Qualitative geometry (SEM).
[38]	2023	Reticular	LPBF	Mechanical integrity (visual inspection).
[39]	2023	Pin fins, plate fins, reticular	LPBF+Spark plasma sintering	Microstructure (SEM); phase analysis (XRD); geometry, defects and pores (μCT); roughness (nominal roughness of the process)
[40]	2023	Manifold microchannels	LPBF	–
[41]	2023	Reticular	n.d.	–

produced structures, 2 only offer a qualitative description of the mechanical integrity and morphological defects [33,34], and 2 measure the actual thermal conductivity of the material [19,24]. Material thermal conductivity is a crucial parameter, and it is worth pointing out that most authors improperly derive it from material and machine supplier datasheets or, in the worst cases, from databases concerning traditional materials. Only 6 articles provide more detailed insights into the structures' geometry, the beams' defects, the surface morphology and roughness, and other important product characteristics. However, the data are scattered, and frequently the conducted tests are not sufficient for providing a precise and complete description of the analysed features. In other cases, unimportant data are presented (e.g. microstructure) or expensive and rarely available tests are performed (e.g. X-ray microtomography (μCT)). All these practices result in a lack of fundamental data for understanding the underlying physics and for ensuring their replicability. Furthermore, the lack of proofs regarding the manufacturability of the developed geometries may incorrectly orient the scientific community on unfeasible solutions.

From the analysis reported above, it is clear that the existing literature is not sufficient for designing novel and practical solutions. Research efforts should be redirected towards optimizing basic designs and providing readily accessible reference data and correlations derived under standard conditions. The present contribution aims to fill this gap by extending and improving the initial exploratory work on the aerothermal performance of Body-Centered Cubic (BCC) lattice structures conducted by the same authors in [7].

In detail, the previous analysis is extended to a wider Reynolds number range and a preliminary shape optimization is also carried out. Here a strict and repeatable experimental procedure was established by:

- performing reliable heat transfer and friction factor measurements across a wide range of Reynolds numbers, not limited to only laminar or fully turbulent conditions;
- comprehensively characterizing the inlet flow conditions, which is crucial for the general validity of the reported results but it is rarely available in the existing literature;
- defining a comprehensive yet lean and cost-effective methodology for characterizing structures produced by AM, including geometrical conformity, surface morphology, surface roughness and material thermal properties that are (surprisingly) frequently neglected.

Actually, multiple features of the original geometries [7] could be varied and optimized, including the lateral or streamwise pitch, struts opening angle, porosity, and more. Nevertheless, the present contribution is focused on the shape variation of the struts' cross section, which was expected to provide a significant performance gain in terms of pressure drops. In the next section, the tested AM components and the improved experimental rig will be described in detail. The inlet flow characterization will be illustrated in Section 3. The final comparison among the different kinds of lattice structures in terms of heat exchange and pressure losses will be presented in Section 4. Eventually, the main findings will be summarized in the conclusions.

2. Experimental methods

2.1. Investigated heat sinks

This contribution is devoted to extending the investigation on other three heat sinks with respect to the previous work [7]; therefore, a total of six heat sinks were characterized in terms of aerothermal performances. The heat sinks have a bulk dimension of 140 × 224 × 30 mm and consist of a periodic arrangement of BCC unit cells of H=10 mm height, which are confined by two base plates with a thickness of 10 mm. The overall dimensions of the test specimens are such to minimize boundary effects and ensure the development of a fully periodic flow in both streamwise and spanwise directions. By so doing the obtained

performance results will have a greater generality, independently from the actual size of the specimen. This approach will enable a more significant comparison among different geometries of the BCC cells. The latter are in a staggered array with the spanwise spacing-to-channel height ratio S_x/H and the streamwise spacing-to-channel height ratio S_y/H equal to 2 and 2.8, respectively (Fig. 1(a)). Four struts with a constant cross-section and intersecting each other in the middle form the BCC unit cell, as is shown in Fig. 1(b). The struts are inclined at 30° with respect to the base plate. The heat sinks differ in terms of the cross-section of the truss in the streamwise plane. Specifically, four shapes have been studied: circular, ellipse, drop, and cam (Fig. 1(c)). For the circular cross-section, three different sizes of struts were considered. These are the three heat sinks that were already characterized in [7]; in the present contribution, their performances were also explored at higher Reynolds numbers and under a different entry flow boundary condition. The other heat sinks have the same flow passage area as those with the circular cross section struts (i.e., they have the same value for the parameter d but a tapered cross-section shape). The geometrical details of the heat sinks are reported in Table 2.

The samples (Fig. 2(a) and (b)) were manufactured according to the same procedures adopted for producing S1, S2 and S3 in [7]. In more details, they were manufactured from AlSi10Mg powder consisting of spherical particles ranging from 10.05 μm (10th%ile) to 48.70 μm (90th %ile) in diameter, and having the following chemical composition: base Al, 9.9 %Si, 0.34 %Mg, 0.12 %O, 0.073 %Fe, 0.007 %C, 0.006 %Ti, <0.03 % of other elements. The raw material was processed by means of a Concept Laser M2 Cusing LPBF machine equipped with a single-mode CW ytterbium-doped fiber laser. The process was carried out under inert argon atmosphere with a residual oxygen level below 0.2 %. To enhance the quality of the products, the exposure process was optimized by subdividing each layer into core surfaces, skin surfaces, and contours that were scanned according to the pattern illustrated in [7]. The adopted process parameters are reported in Table 3.

Special specimens for examining the geometric and surface properties of the S4–S6 BCC configurations were prepared using the same manufacturing procedures and conditions adopted for the heat sinks (Fig. 2(c)). These specimens were consistent with those produced in the previous work [7] for the S1–S3 configurations and were subjected to the same manufacturing procedures. Consequently, only the properties of the newly examined structures will be discussed in the following section.

2.2. Characterization of the Body-Centred Cubic (BCC) lattice

In this section, the geometric and surface properties of the S4–S6 BCC configurations are discussed, while the same data concerning the S1–S3 structures are available in [7], where also the inspection procedures are described in more detail.

The samples' geometry was analysed using a 7-axis Romer absolute arm equipped with a Hexagon RS5 laser scanner. The obtained results

Table 2
Heat sink dimension and characteristics.

Heat sink	S1 Circular	S2 Circular	S3 Circular	S4 Ellipse	S5 Drop	S6 Cam
H/d	3	4	5	4	4	4
r/H	–	–	–	–	0.015	0.015
a/H	–	–	–	0.0375	0.0391	0.0391
Flat channel surface area [m^2]	0.0591 (67.4 %)	0.0607 (73.0 %)	0.0614 (77.0 %)	0.0597 (69.1 %)	0.0601 (69.3 %)	0.0597 (69.0 %)
Struts surface area [m^2]	0.0286 (32.6 %)	0.0224 (27.0 %)	0.0184 (23.0 %)	0.0267 (30.9 %)	0.0266 (30.7 %)	0.0269 (31.0 %)
Total wet surface area [m^2]	0.0877 (100 %)	0.0831 (100 %)	0.0798 (100 %)	0.0864 (100 %)	0.0867 (100 %)	0.0866 (100 %)

are presented in Fig. 3 and summarized in Table 4. The probability density functions of the dimensional error is considerably different across the three investigated cases. Specifically, the dimensional error affecting the sample S4 was approximately normally distributed, with a slight positive skewness, while the other cases exhibited a trimodal distribution with two anomalous peaks on either side of the main peak representing the random error. An in-depth investigation proved the concentration of negative errors in between the two BCC cells of each sample and the concentration of positive errors on the opposite sides. The magnitude of the error appeared to increase moving away from the center of the sample, suggesting that the 2D printed slices were stretched around it. This effect may be attributed to the imperfect calibration of the laser optical system, and its impact may vary across the building platform, resulting in different distributions in the three cases. The maximum recorded deviations ranged from 0.328 mm to 0.334 mm, while it was less than 0.1 mm for the S1–S3 samples that were previously tested. Thus, the dimensional error can be about 0.2 mm, and it possibly hid the dross formation on the overhanging surfaces, which was observed on the previously tested samples, while it was apparently irrelevant in the current case. Nevertheless, the shape of beams' cross section was not dramatically distorted: the absolute mean deviation was about 0.05 mm and more than 96 % of the measured points were characterized by an absolute error smaller than 0.25 mm. Since these moderate dimensional errors have a negligible impact on the final behavior of the tested specimens, they can be tolerated and the developed structures were considered suitable for the investigations presented here as well as for some real industrial applications.

The surface morphology was examined using a Sensofar S neox Five Axis 3D confocal microscope featuring a green light source with a wavelength of 530 nm and a Nikon EPI 5x objective. Specifically, the flat surface and the overlaying trusses were scanned parallel to the

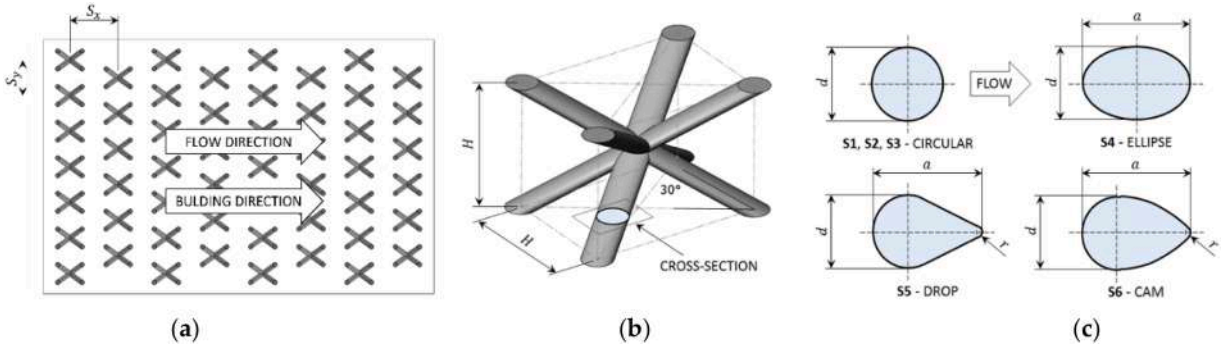

Fig. 1. Heat sinks geometry: (a) arrangement of the unit cells; (b) BCC unit cell; (c) investigated strut cross-sections.

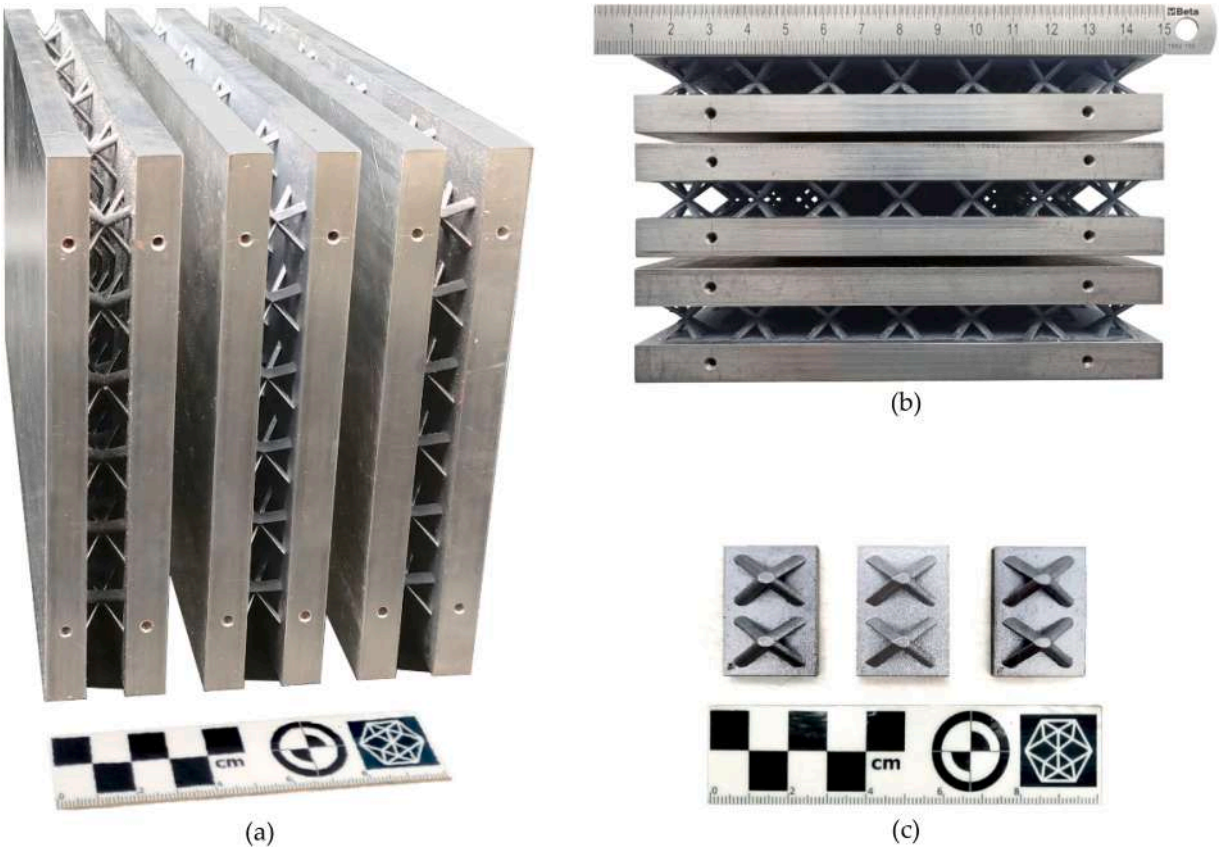

Fig. 2. Samples produced and tested in this study from (a) the outlet side and (b) the inlet side. In (c) the sectioned samples for geometric and surface characterization are shown.

Table 3
Process parameters used for producing the samples.

	Core surface	Skin surface	Contour I pass	Contour II pass
Power	370 W	200 W	200 W	200 W
Scanning speed	1400 mm/s	800 mm/s	1250 mm/s	350 mm/s
Spot diameter	190 μm	140 μm	100 μm	50 μm
Layer thickness	50 μm	25 μm	25 μm	25 μm
Hatch distance	0.112 mm	0.112 mm	–	–

microscope imaging plane capturing 14 × 12 field-of-views measuring 3378.24 × 2826.24 μm^2 each. These scans were then stitched together imposing a 30 % overlap to obtain the final detailed point cloud. The in-plane sampling distance and the focal planes distance were set at 1.38 μm and 12 μm, respectively, while the in-plane and the vertical resolution were 1.08 μm and 100 nm, respectively. The light brightness and the microscope sensitivity were systematically optimized to minimize the image dark spots. According to ISO/IEC guide 98–3:2008 GUM:1995, the measurement accuracy exceeded 600 nm (95 % level of confidence) while the measurement repeatability exceeded 20 nm. The results obtained after flattening a restricted region of 1 × 1 mm^2 in size by applying the linear areal Gaussian filter ($\lambda_{c,FALG}$= 1.144 mm) defined in the standard ISO 16,610–61, and cancelling any signal anomalies by using dedicated statistical filters, are presented in Fig. 4. No appreciable differences were observed across the samples analyzed in this (S4–S6) and prior research (S1–S3). Also in this case, the flat walls were flawless and uniform, while the beams were affected by localized outgrowths and depressions, as well as by low frequency ripples which were caused by thermal shrinkage and stresses induced by the production process. The defects were found to be more frequent and prominent on the lower skins.

Finally, the data obtained by confocal microscopy were used to measure the Roughness average Ra and the Waviness average Wa of the flat walls and the trusses. In more detail, signal anomalies were remoced from each point cloud by using dedicated statistical filters, and 7.2 mm long surface profiles were extracted from the center line of the flat walls and from each truss, where the roughness was intermediate compared to the extreme values observed at the edges built with different overhang angles. The obtained data were then processed according to the standard ISO 4287 adopting two cut-off wavelengths, namely λ_c=0.8 mm and λ_c=1.2 mm. The former is recommmended when standard prescriptions cannot be met, while the latter results in five sampling length available in the 7.2 mm evaluation length and was considered suitable for analyzing the surfaces of parts produced via LPBF [42]. The results summarized in Table 5 revealed a significant correlation between Ra and the cut-off wavelength, the samples geometry and the skin orientation. Specifically, Ra was found to be higher on average by 14.8 % for λ_c=1.2 mm, and Ra(λ_c=1.2 mm) was higher on average by 21.9 and 20.7 % for the bulkier trusses (elliptical cross-section) and the down-skins, respectively. The skin orientation also impacted Wa which was lower on average by 51 % on the down-skins. However, when considering the data from the prior research, the main effect of truss geometry on Ra is no more significant, suggesting that the variability due to this factor is comparable to or lower than the inherent variability caused by this manufacturing technology. Conversely, Wa appeared to be significantly affected by the samples' geometry and not by the skin orientation. This is because an opposite correlation between Wa and the skin orientation was observed in [7], presumably because of the different trusses' geometry. A statistically significant interaction between trusses' geometry and skin orientation was also found (p-value=6 × 10^{-15}). Lastly, both Ra and Wa were minimal on vertical surfaces. In conclusion, it can be inferred that Ra only depends on the trusses'

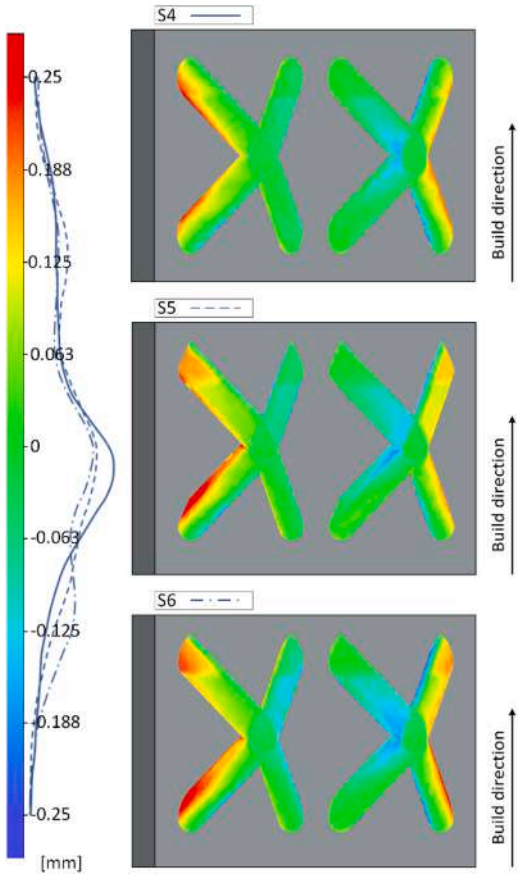

Fig. 3. Dimensional error of the S4, S5, and S6 BCC configurations obtained by inspecting special sectioned samples with a portable laser scanner.

Table 4
Samples conformity obtained by laser-scanning.

Sample	Absolute mean deviation	Dispersion(Standard deviation)	Maximum deviation
S4	0.048 mm	0.074 mm	0.334 mm
S5	0.052 mm	0.081 mm	0.325 mm
S6	0.053 mm	0.085 mm	0.328 mm

inclination, while Wa depends on both trusses' inclination and geometry.

Finally, the thermal properties of the LPBF material were measured in [43] by using the hot disk transient plane source method and special samples manufactured by the authors of the present paper using the same machine, powder, process parameters and procedures. The average results of five repeated measurements are reported in Table 6.

2.3. Test facility and data reduction

In Fig. 5 the upgraded test rig used to measure the aerothermal performances of each heat sink is illustrated. Its design and characteristics are thoroughly described in the previous contribution [7]. For this reason, only its main features and differences with respect to the previous test facility will be highlighted here.

The test facility is composed of three sequential sections: inlet section, test section, and air suction system. The air is sucked from the room condition through a honeycomb filter and a 9:1 contraction. Then the air flows through the feeding channel, which is a straight rectangular channel with a 140 × 10 mm^2 cross-section area (same dimensions as those of the heat sinks). With the aim to provide experimental data obtained in meaningful and reproducible boundary conditions, it was decided to ensure a fully developed flow at the test section entry. The hydrodynamic entry length could be derived from Eq. (1) for the laminar flow (limiting case of $Re = 2'300$) [44], otherwise for turbulent flow it can be assessed from Eq. (2).

$$L/D_h \approx 0.05\ Re \tag{1}$$

$$L/D_h \approx 10 \tag{2}$$

The most stringent condition is dictated by the required entry length in the laminar region, which turns out to be at least 115 L/D_h in the upper limit of the correlation. This prescription was not respected in the previous version of the experimental facility ($L = 27D_h$); therefore, the feeding channel has been lengthened by $128D_h$ in order to achieve a total length of $155D_h$. An exhaustive discussion about the entry conditions obtainable through the adoption of such feeding channel are presented in the Section 3 - "Inlet flow characterization". At the end of the feeding channel, 2 K-type thermocouples are immersed in the core flow and monitor the inlet flow temperature. Futhermore, 4 pressure taps are present around the cross-section of the channel to measure the inlet static pressure. Then, the air passes through the heat sink and is driven into the settling chamber through a connection channel with a cross-section of 140 × 10 mm^2 (the same as the feeding channel). At the beginning of this channel (i.e., imminently at the exit from the heat sinks), other 4 pressure taps collect the outlet statics pressure. ~~and,~~ Immediately downstream, a 5:1 contraction of the channel is made. 4 K-type unshrouded thermocouples are mounted in the throat section of the contraction in order to evaluate as close as possible the outlet bulk flow temperature (see Figs. 5 and 7). The inlet and outlet air static temperatures (T) were computed from the temperature values read by the thermocouples (T_{read}, both at the inlet section and at the throat section) corrected from the velocity error by means of the recovery factor (Rec), Eq. (3), [45].

In Eq. (3), the velocity is computed as a bulk velocity ($U_b = \dot{m}/A_c\rho$) with the local flow properies at the location of the channel where the termocouples are inserted (i.e. immediately upstream of the test section and in the throat of the outlet nozzle, see Figs. 5 and 7). The recovery factors at different flowrates were estimated by varying this parameter during an *in-situ* calibration test.

$$T = T_{read} - Rec\left(\frac{U_b^2}{2c_p}\right) \tag{3}$$

Typical values of the recovery factor were ranging from 0.76 at *Re* 30.000 to 0.87 at *Re* 2.500, the lowest values obtained a the outlet where a maximum Mach number of about 0.4 was reached (precisely, at the nozzle exit). This implied a slight difference of about 10 °C between the read and the corrected temperatures.

Eq. (3) will therefore be used to estimate ~~obtained~~ the inlet and outlet flow temperatures, main inputs for computing the Nu number, as it will be clarifed later on in the discussion (see Eqs. (11) and (12)). In particular the T_{OUT} values are obtained from the corrected flow temperaures at the contraction nozzle exit ($T_{OUT,C}$) by assuimg a flow evolution at constant total enthalpy (i.e. by neglecting energy losses towards the enviroment during the expansion inside the nozzle, Eq. (4)), that is

$$T_{OUT} + \frac{U_{b,OUT}^2}{2c_p} = T_{OUT,C} + \frac{U_{b,OUT,C}^2}{2c_p} \tag{4}$$

Then, the air is taken from the settling chamber and two centrifugal fans force the flow through one of the two parallel flow meters installed in the system. Two different flow meters are necessary for accurate measurements at high (orifice plate flow meter) and low mass flows (vortex flow meter). In the previous version of the test facility, only the vortex flow meter have been used for flowrates up to 100 kg/h and only one centrifugal fan was necessary. With the additional fan and the orifce

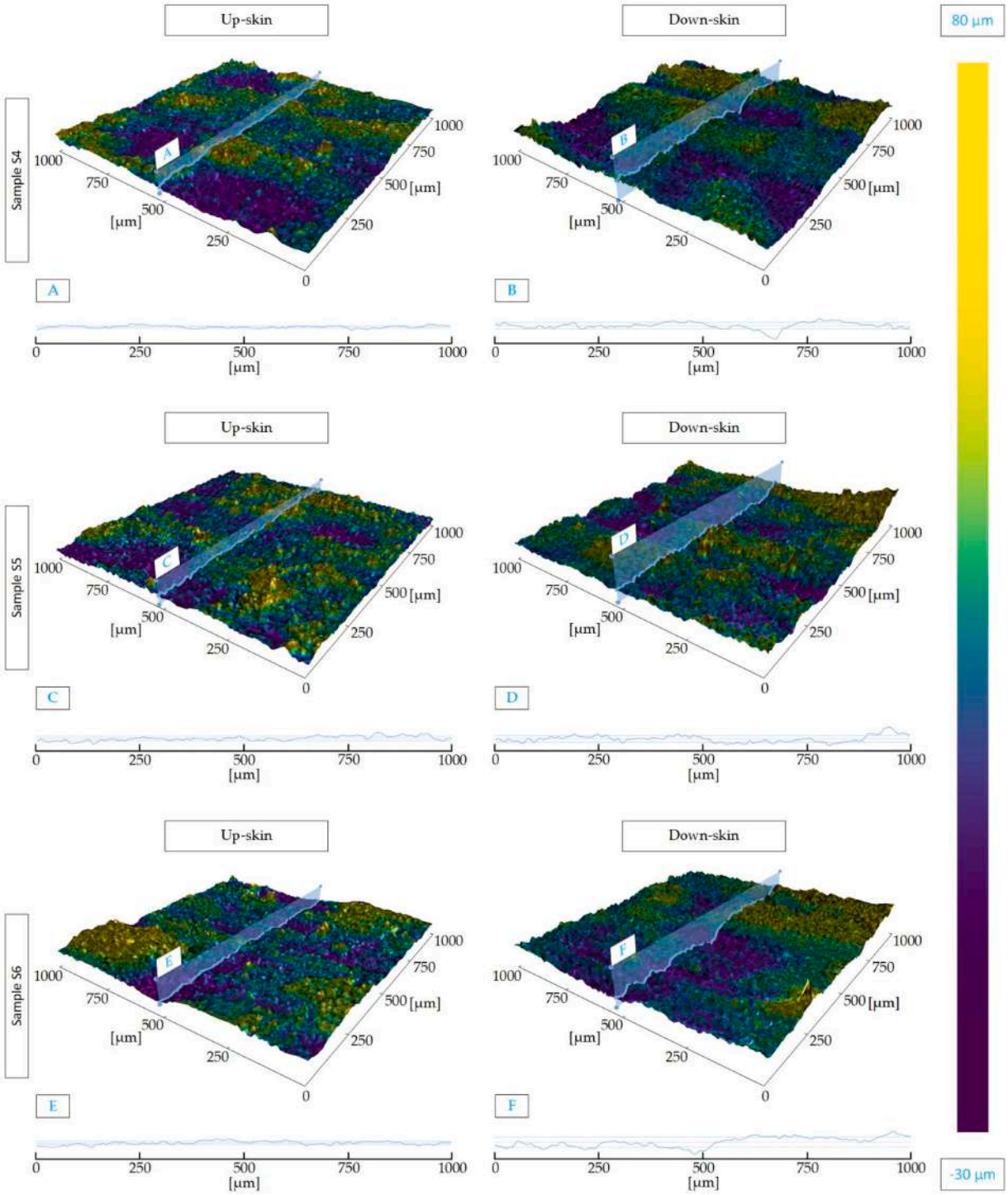

Fig. 4. Surface morphology of the trusses inspected by a confocal microscope (note that the coloured maps scaling differs from the in-plane scaling to emphasize defects).

flow meter, the investigated flow regimes could be extended up to a Reynolds number of 30′000.

During heat transfer experiments (see Fig. 6), a unifom heat flux was supplied to both the upper and lower surface of the heat sink, by means of two electrical resistance surface heaters (i.e., 25 µm thick Inconel foils). The resistance foils adhered to aluminum blocks of 20 mm thickness by interposing a layer of paper sheet with temperature resistance up to 220 °C in order to electrically insulate the two metals. The Inconel foils was electrically fed by a DC power supply, and the input heat was calculated by means of Eq. (5) from the measured values of the current and of the voltage drop across the heaters.

$$Q_{el} = EI \tag{5}$$

The instrumented blocks lie on the external faces of the heat sinks and a good thermal contact was ensured by a thin layer of thermal paste. 24 T-type thermocouples were embedded in specific positions throughout the aluminium blocks (Fig. 6(b)). These thermocouples together with those that monitor the temperature of the air flow were calibrated in a thermal bath and within the working range in order to ensure a low relative error.

Table 5
Mean values of the Roughness average *Ra* and the Waviness average *Wa* measured on the flat wall and the trusses.

	Ra (λ_c=0.8 mm) [μm]		*Ra* (λ_c=1.2 mm) [μm]		*Wa* (λ_c=0.8 mm) [μm]		*Wa* (λ_c=1.2 mm) [μm]	
	Mean	Standard deviation	Mean	Standard deviation	Mean	Standard deviation	Mean	Standard deviation
Flat walls	4.73	0.57	4.94	0.63	2.58	0.93	2.36	1.06
S4 (ellipse) up-skins	3.58	0.32	4.38	0.16	15.09	1.88	14.87	1.99
S4 (ellipse) down-skins	5.15	0.70	6.14	0.76	11.14	2.68	10.65	2.30
S5 (drop) up-skins	3.27	0.07	3.91	0.07	15.60	1.61	15.12	1.66
S5 (drop) down-skins	4.55	0.38	5.32	0.26	12.53	2.02	11.86	2.09
S6 (cam) up-skins	3.61	0.41	4.62	0.29	19.56	0.70	19.20	0.90
S6 (cam) down-skins	3.93	0.59	4.45	0.71	10.63	2.63	9.83	2.67

Table 6
Thermal properties of the LPBF processed material [43].

Thermal properties	AlSi10Mg
Thermal conductivity	175 W/(mK)
Thermal diffusivity	73.8 mm^2/s

The thermocouples that measure the temperatures inside the aluminum blocks allowed for the estimation of the internal surface temperatures of the heat sinks by means of 1D conduction analysis (Eq. (6)). The overall thermal resistance (R) is estimated by the series of thermal resistances, that are shown graphically in Fig. 7. The thermal conductivity of the aluminium plate was derived from the vendor's datasheet and that of the samples material can be obtained from [43], where the conductivity and diffusivity were experimentally measured through the hot disk transient plane source method. The Authors in [43] manufactured samples according to the same production cycle and by using the same equipment, powder, parameters and procedures of the current contribution. The contact resistance was negleted from the computation of the overall resistance, since all the components of the heating system are strongly pressed together with the test section in between and a thermally conductive paste is used at the interface.

$$T_w = T_{Al} - RQ_{el} \tag{6}$$

Eq. (6) was used to compute the actual temperature of the wall touched by the flow, which was then used to compute the Nusselt number, as it will be explained at the end of this section (see Eqs. (11) and (12)).

As shown in Fig. 7, the assembly was compressed vertically by enforcing an external pressure through two MDF panels (with interpose a 3 mm thick foil of thermal insulating material) and several screw jacks (in Fig. 6(a) the MDF panel and the Inconel foil on the top are removed). Additionally, the test section was isolated from the external environment by a thick layer of rock wool which minimized the thermal losses. The energy balance between input electric power and the power drawn by the air:

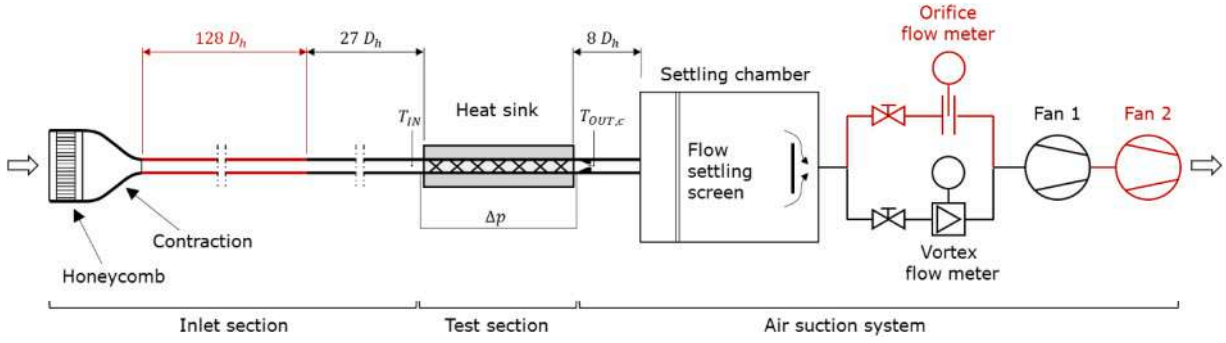

Fig. 5. Heat sink test apparatus (in red the updates with respect to the previous rig [7]).

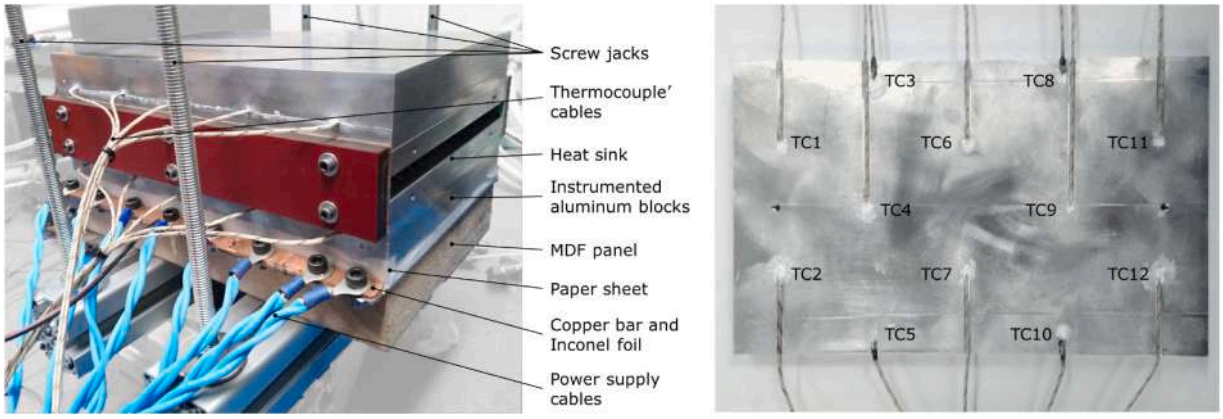

Fig. 6. Test section: (**a**) instrumentation for heat transfer measurements (in this view the MDF panel and the Inconel foilon the top are removed); (**b**) aluminium plate with the thermocouples (TC) installed.

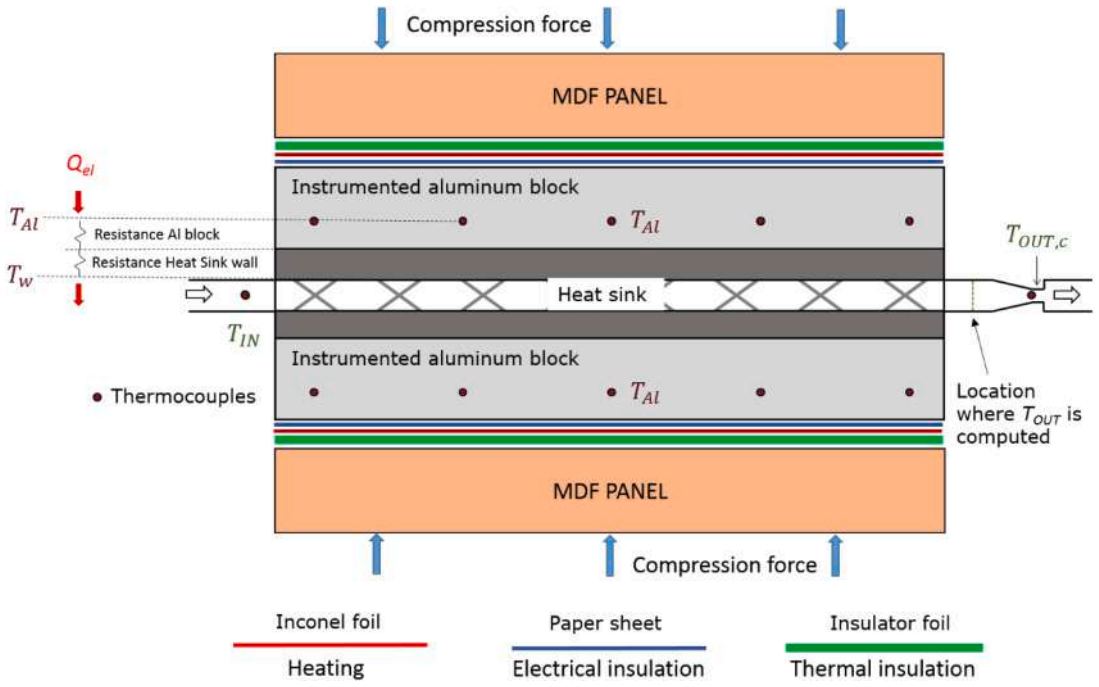

Fig. 7. Cross section view of the test stack used in the heat transfer investigation.

$$Q_{air} = \dot{m}\left(h_{0,OUT} - h_{0,IN}\right) \tag{7}$$

was calculated for each heat sink and test condition. As shown in Fig. 8, the energy balance is always within ±5 % for the majority of the tests, only in few cases the residual of the energy balance rises to ±9 %. This proves the good thermal insulation of the test sections.

All the thermal performances are evaluated in terms of dimensionless parameters. These dimensionless groups are computed on a reference length that is the empty channel hydraulic diameter (D_h) defined in Eq. (8). In more detail, the friction factor (f) and the Nussel number (Nu) are used to represent the pressure drop and the heat transfer coefficient of each heat sink as a function of the inlet Reynolds number (*Re*) specified in Eq. (8).

$$D_h = \frac{4A_c}{P} \tag{8}$$

$$Re = \frac{\rho U_b D_h}{\mu} \tag{9}$$

The friction factor (f) is computed by using the pressure drop, see Eq. (10). A water column micromanometer was employed to measure the pressure differences across the heat sinks and the tests were conducted without heating the surfaces of the heat sinks in order to exclude the effects of temperature-dependent air properties.

$$f = \Delta p \frac{D_h}{\Delta L} \frac{2}{\rho U_b^2} \tag{10}$$

In the heat transfer investigation, the measurements were acquired over a steady-state 5 min interval every 3 s. The steady thermal condition was considered reached when the values of the termocouples inserted in the aluminum blocks were stable over a time interval of at least 15 min, after which the data logging started. The Nusselt number (Nu) was calculated by Eq. (11), where A_r is the reference surface area (equal to 140 × 224=31,360 mm^2) and ΔT_{ml} is the log mean temperature difference defined in Eq. (12). In this way, the heat transfer coefficients describe the heat transfer augmentation from the walls and they represent the global heat transfer performances of the heat sink.

$$Nu = h\frac{D_h}{k} = \frac{Q_{el}}{A_r\ \Delta T_{ml}} \frac{D_h}{k} \tag{11}$$

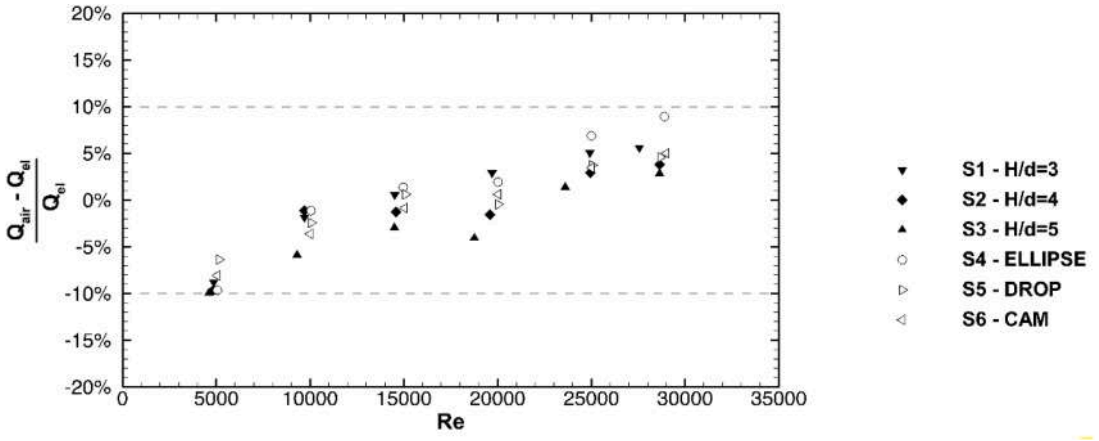

Fig. 8. Power balance for the heat sinks as a function of the inlet Reynolds number (see Eq. (9)).

$$\Delta T_{ml} = \frac{T_{OUT} - T_{IN}}{\ln\left(\frac{T_{OUT}-T_w}{T_{IN}-T_w}\right)} \tag{12}$$

Concerning the estimation of the experimental uncertainty for the performace parameters, the same approach used in [7] was applied and commented in the appendix. For the sake of brevity, only the upper estimates that applies to the heat sink cases are reported here. Specifically, the uncertainty is below 3.8 % for the Reynolds number, below 15 % for the friction factor and below 9.5 % for the Nusselt number.

3. Inlet flow characterization

3.1. PIV investigation

The detailed investigation of the inlet conditions resulting from the adoption of the previous $L = 27D_h$ [7] and the current $L = 155D_h$ feeding channel was performed using a 2D Particle Image Velocimetry technique. Fig. 9 shows the PIV setup and the location of the measurement plane: the experimental analysis was focused on the vertical symmetry plane of the feeding channel, with a field of view that covers the space between $8D_h$ and $2D_h$ upstream of the entry section of the heat sink.

A pulsed two-cavity Nd-YAG laser source capable of depositing 120 mJ of energy per pulsation operating at a wavelenght of 532 nm generated the laser sheets necessary to illuminate the tracer particles. The tracer particles were produced by a Laskin nozzle-type seeding generator and consisted of a vegetable oil aerosol with a monodisperse distribution around 1.2 μm. The 12-bit camera FlowSense EO 4M-32 with a spatial resolution of 2072 × 2072 pixels equipped with Nikon lens of 60 mm focal length was used for image recording with a magnification factor of about 140 pix/mm. The PIV measurement chain (i.e., laser pulses and camera acquisition) was synchronized through the Timer Box of Dantec PIV system. A sample frequency of 10 Hz was set to collect 1′000 pairs of images for each investigated flowrate condition, namely Re = {5′000; 6′000; 6′750; 10′000; 20′000; 30′000}. After data acquisition, the pairs of PIV frames were processed and cross-correlated by using the commercial software Dynamic Studio 2016a. The images were pre-processed for removing the background image, which is the result of the min intensity values of each pixel of the image ensemble. Than a multy-size window refinement method was perfomed to cross-correlate each pair of images with a final window size of 16×16 pixles. The resulting spatial resolution of the velocity fields is therfore 8.75 vectors/mm, thus adequate to characterize the flow boundary layer. The uncorrelated instantaneous flow fields were averaged to obtain the mean velocity and velocity fluctations fields. As a final remark, it has to be specified that thanks to the large number of samples (1000) used to compute the time averaged flow fields, a rather good convergence of the statistics is achieved, with an accuracy of the computed mean values of less than 2 % of U_b (95 % of confidence interval). More details about this aspect are provided in appendix.

In the folowing, for the sake of clarity only the flow field data extracted along Z-direction at $X = -3D_h$ will be presented. Futhermore, only half channel is reported given the symetrical flow condition. Figs. 10–15 show the streamwise velocity (U), streamwise velocity fluctuations (U'), and crosswise velocity fluctuations (W') for all the tested conditions. All these quantities are reported in a normalized form using the bulk velocity (U_b) as reference value.

The adoption of the two entry lenghts causes a large difference in the velocity distribution at Re = 5′000, 6′000, and 6′750. Then, for higher flow rates ($Re \geq 10'000$), the velocity profile discrepancy drops below 4 %, until the two flow distributions are practically overlapped at Re = 30′000. Similar considerations can be made about the velocity fluctation profiles. Also in this case, the fluctuation values are extremely different for $Re \leq 6'750$ and show similar trends in the other flow conditions. These observations clearly demostrate how the adoption of feeding channels with $L = 27D_h$ or $L = 155D_h$ produces two distinct flow evolutions and, consequently, different inlet conditions for the heat sinks. In other words, the flow transition occurs at different Reynolds numbers in the two facility configurations. In order to evaluate the achievement of the fully developed flow condition, the PIV flow data are compared with those obtained from the Direct Numerical Simulation (DNS) of Iwamoto et al. [46]. The Authors in [46] simulated the flow field driven by a streamwise mean pressure gradient in a fully-developed turbulent flow between two parallel walls. They studied different flow conditions that were evaluated at the Reynolds number defined by Eq. (13).

$$Re_{DNS} = \frac{\rho U_b H}{\mu} \tag{13}$$

It is worth noting that the characteristic scale length used to compute the Re_{DNS} values characterizing the simulations is different from that used in the current paper (i.e., channel height instead of the hydraulic diameter of the channel). Table 7 reports the available flow conditions in the dataset [46] and the relative Reynolds number values recalculated according to the definition used in this work. In the same table, the corresponding Re of the PIV experiments associated for the comparison is also given.

The closest flow conditions available in the DNS database are compared to those investigated in the PIV campaign, as reported with the black continuous line in Figs. 10–15. The velocity distribution obtained with an entry channel of $L = 27D_h$ presents similar trends with

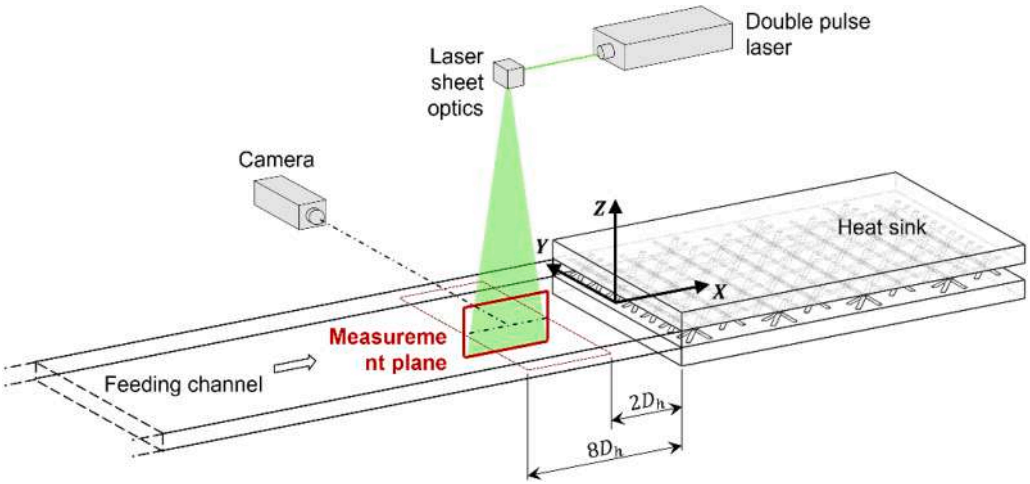

Fig. 9. Particle image velocimetry setup and position of the measurement plane.

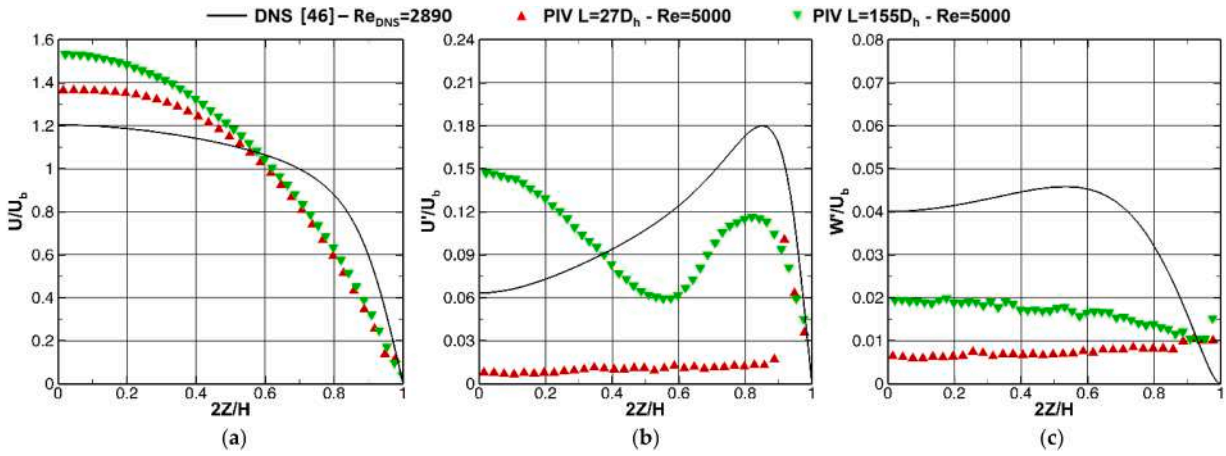

Fig. 10. Flow field results extracted at $X = -3D_h$ for $Re = 5'000$: (a) normalized streamwise velocity; (b) normalized streamwise velocity fluctuations; (c) normalized crosswise velocity fluctuations;.

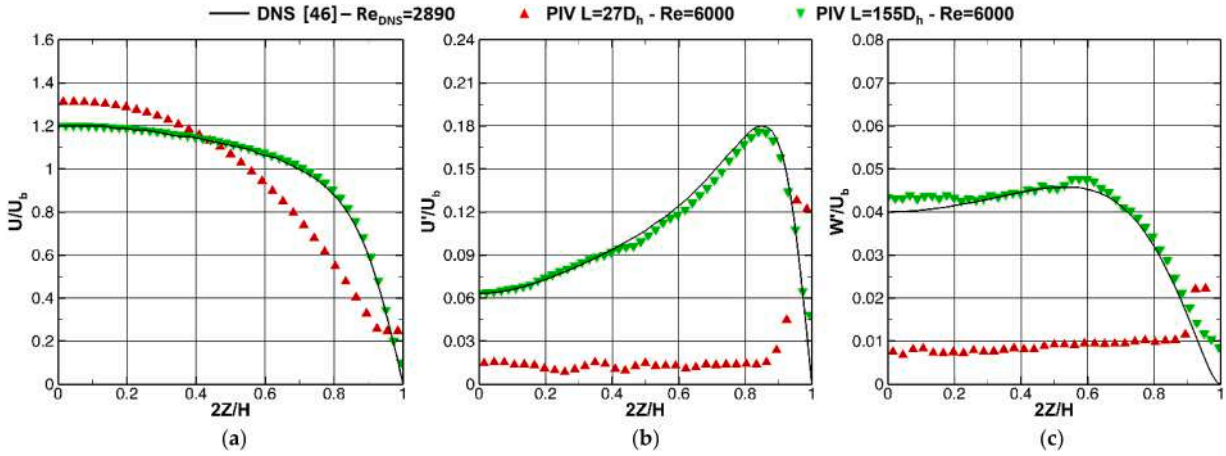

Fig. 11. Flow field results extracted at $X = -3D_h$ for $Re = 6'000$: (a) normalized streamwise velocity; (b) normalized streamwise velocity fluctuations; (c) normalized crosswise velocity fluctuations;.

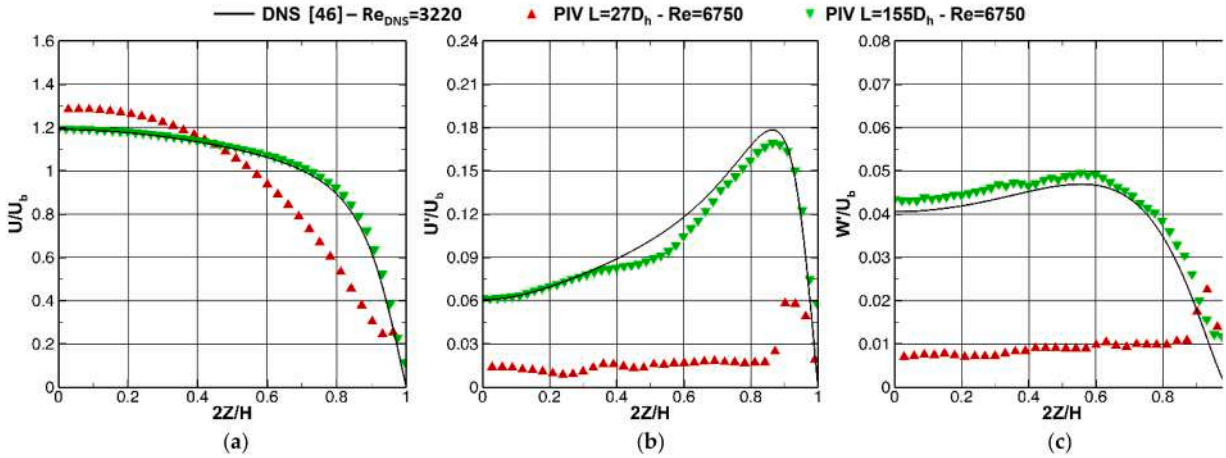

Fig. 12. Flow field results extracted at $X = -3D_h$ for $Re = 6'750$: (a) normalized streamwise velocity; (b) normalized streamwise velocity fluctuations; (c) normalized crosswise velocity fluctuations;.

those of a fully developed flow starting from $Re = 10'000$. Instead, by using the longer channel with $L = 155D_h$, a fully developed flow is obtained already at $Re \geq 6'000$. At Re=5′000, the flow is in full transition, as demonstrated by the profile of the streamwise velocity

3.2. Pressure losses of the smooth channel

As it is well known, the friction factor of the smooth channel (f_0) is not the most suited parameter for characterizing the flow conditions;

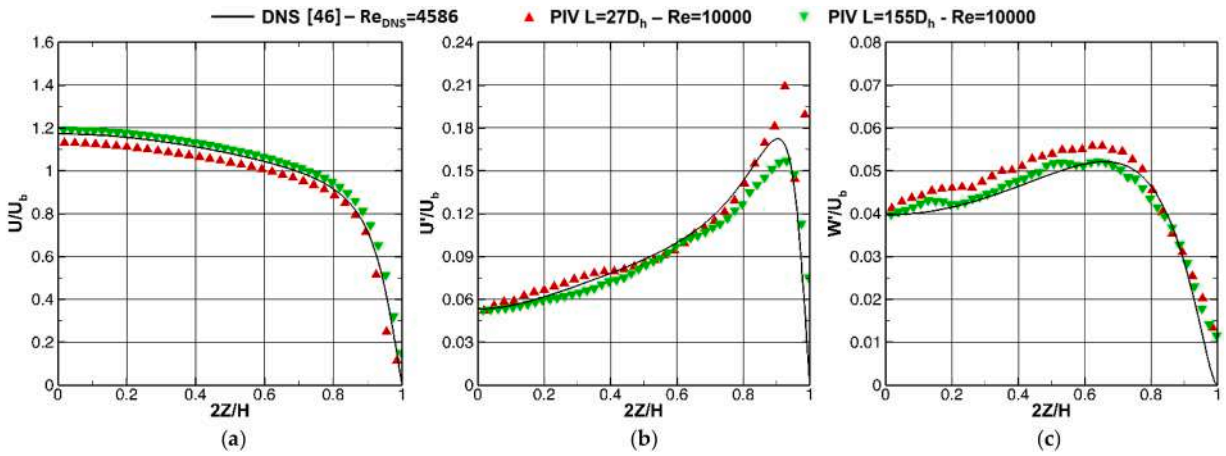

Fig. 13. Flow field results extracted at $X = -3D_h$ for $Re = 10'000$: (a) normalized streamwise velocity; (b) normalized streamwise velocity fluctuations; (c) normalized crosswise velocity fluctuations;.

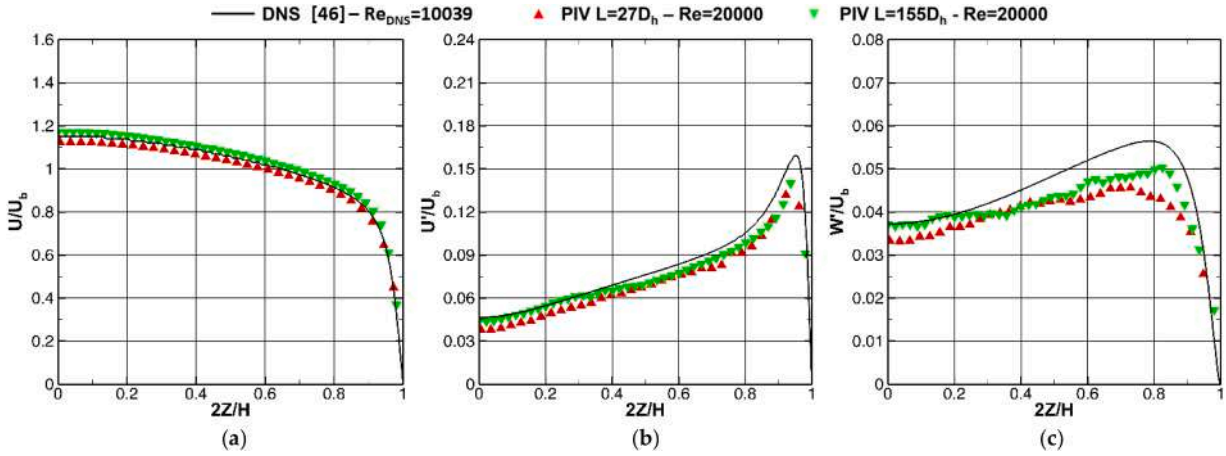

Fig. 14. Flow field results extracted at $X = -3D_h$ for $Re = 20'000$: (a) normalized streamwise velocity; (b) normalized streamwise velocity fluctuations; (c) normalized crosswise velocity fluctuations;.

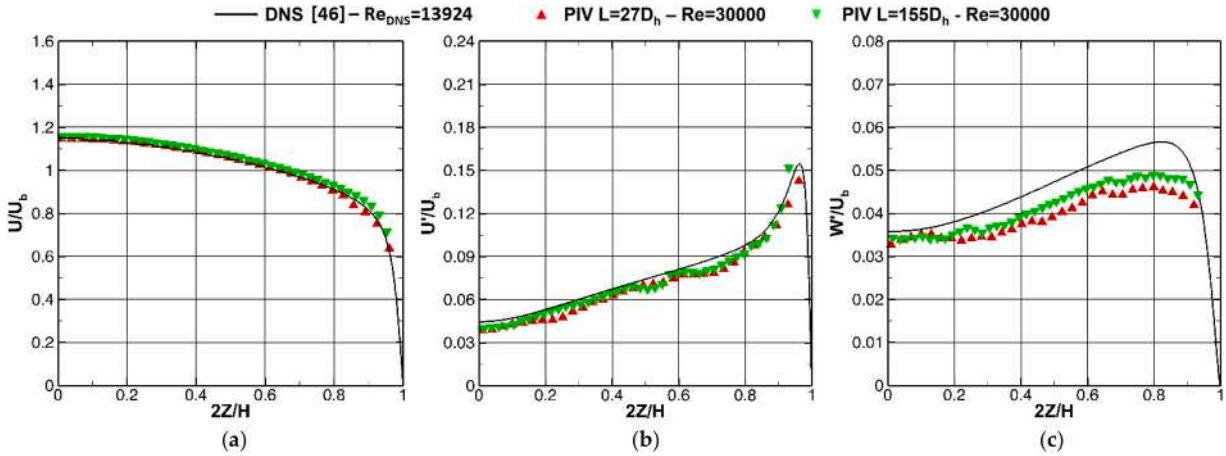

Fig. 15. Flow field results extracted at $X = -3D_h$ for $Re = 30'000$: (a) normalized streamwise velocity; (b) normalized streamwise velocity fluctuations; (c) normalized crosswise velocity fluctuations;fluctuations provied in Fig. 10. From Re=6′000 (Fig. 11) and up to the maxiumm value considered here (Figs. 12-15), the PIV data for the longer entry length channel ($L = 155D_h$) are fully comparable with those reported by the DNS simulations both in terms of averaged and fluctuating velocities.

however, its value at different Reynolds numbers is also sensitive to the different entry lengths. Also, friction factor data for the smooth channel will be used in the next sections to comment about the performances of the BCC considered here and therefore it is given in Fig. 16. In the figure, the results obtained for the smooth channel having length $L = 27D_h$ [7] are compared to those obtained with the longer feeding channel having

Table 7
Flow conditions that are available in the DNS dataset of [46].

DNS		PIV
Re_{DNS}	Re	Re
2′890	5′395	5′000
2′890	5395	6′000
3′220	6′012	6′750
4′586	8′562	10′000
10′039	18′743	20′000
13′924	25′998	30′000

length $L = 155D_h$. Additionally, correlations from the literature are provided for the sake of completeness. For the laminar flow, the friction factor is computed as $f = 96/Re$ [44], while for the turbulent flow conditions the Colebrook- White equation is widely assumed as a good refence [47]. However, this equation is implicit in f and, therefore, the well-known approximation from Haaland [48] has been adopted:

$$\frac{1}{\sqrt{f}} \cong -1.8\log\left[\frac{6.9}{Re} + \left(\frac{\varepsilon/D_h}{3.7}\right)^{1.11}\right] \tag{14}$$

where $\frac{\varepsilon}{D_h}$ was set to 0.006 in the current case. As illustrated in Fig. 16, both f_0 trends obtained from the two configurations present similar characteristics. For low Reynolds numbers, the f_0 values are in accordance with the laminar correlation, while at high Reynolds numbers they are close to the typical values of a turbulent flow. The major differences are noticed in the transition zones from laminar to turbulent conditions. For the smooth channel with the shorter entry length the fully turbulent flow is achieved at $Re \approx 12'000$, whereas it occurs at $Re \approx 6'000$ for the longer feeding channel.

The data reported in Fig. 16 confirm the results derived from PIV measurements. For this reason, the Reynolds numbers investigated by means of PIV are indicated by the dashed vertical lines in the same figure. At $Re = 5'000$ none of the 2 feeding channels leads to the fully developed flow condition, as attested by the values of f_0 and the velocity profiles reported in Fig. 10. For the channel with $L = 155D_h$ and at $Re = 6'000$, the velocity distribution is consistent to that of a fully developed turbulent flow (see the comparison of PIV and DNS data in Fig. 11) and indeed the value of f_0 reflects the value predicted by the classic turbulent correlation. On the contrary, for the shorter channel it is necessary to reach $Re > 10'000$ to achieve a fully developed condition (Figs. 14 and 15) and a friction coefficient close to the value predicted by the turbulent correlation.

4. Results and discussion

4.1. Heat sinks with circular cross-section

The aero and thermal performance measured for the three heat sinks with struts of circular cross section are reported in Fig. 17. The plots include also the results obtained in the previous investigation [7], that were limited to Re=20′000 and extended up to 30′000 in the present contribution. At first, it can be observed that the agreement between previous and present data of both friction factor and Nu number is very good. This facts confirms the reliability and repeatability of the proposed experimental rig and methodology. Also, they confirm that the inlet flow conditions have a negligible impact on the final performances of the heat sinks. Boundary layer characteristics and turbulent content of the approaching flow are overwhelmed by the turbulence promoted by the first row of BCC which influences the downstream development of the flow and the thermal fields.

The monotonous increase of heat exchange with the Reynolds number is confirmed. The sample with the larger struts diameter (S1) reports Nu values up to 300 at Re=30′000, a value that is almost 150 % higher than the sample with the smallest diameter (S3). At the same time, it determines the highest friction losses in view of the larger blockage effect and wetted surface.

In the previous work [7] a correlation was proposed to estimate the circular cross section BCC performances, and it is here extended up to Re=30′000 by including the new results. The correlation is defined by normalizing the aero and thermal performances' data by $D_{BCC} = 4\,V_w/A_w$, which is the hydraulic diameter of the non-uniform cross--section areas [49]. The further correction by the ratio D_h/d allows accounting for scale effects (the actual size of the internal structure with respect to the empty channel characteristic length). Thus, modified versions of the Nusselt number, Reynolds number and friction factor were defined as follows:

$$Re^* = Re\left(\frac{D_{BCC}}{d}\right) = \frac{\rho v D_{BCC}}{\mu}\left(\frac{D_h}{d}\right) \tag{15}$$

$$f^* = f\left(\frac{D_{BCC}}{d}\right) = \Delta p \frac{2}{\rho v^2}\frac{D_{BCC}}{\Delta L}\left(\frac{D_h}{d}\right) \tag{16}$$

$$Nu^* = Nu\left(\frac{D_{BCC}}{d}\right) = h\frac{D_{BCC}}{k}\left(\frac{D_h}{d}\right) \tag{17}$$

The aerothermal performances of the three different heat sinks with circular cross-section are eventually represented by the modified Nusselt number (Eq. (17)) and by the modified friction factor (Eq. (16)), which are expressed as functions of the modified Reynolds number (Eq. (15)).

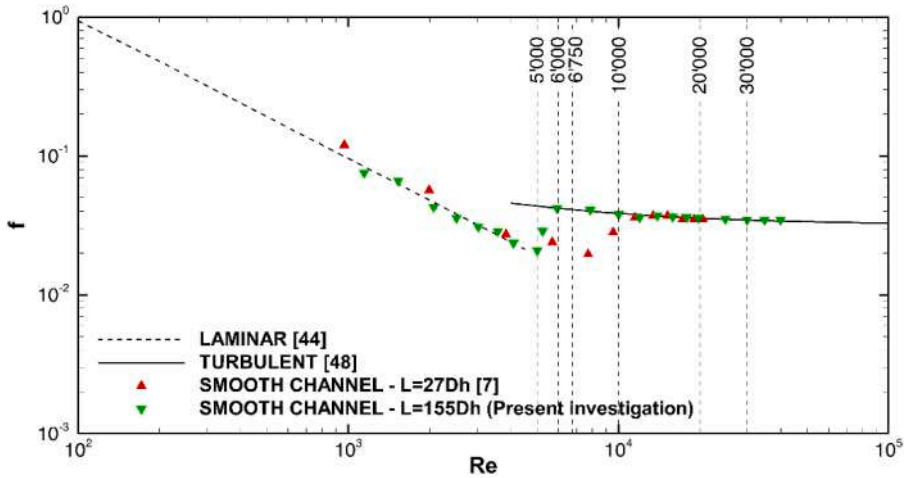

Fig. 16. Friction factor of the smooth channel in the 2 system configurations: feeding channel of $L = 27D_h$ (in red) and $L = 155D_h$ (in green).

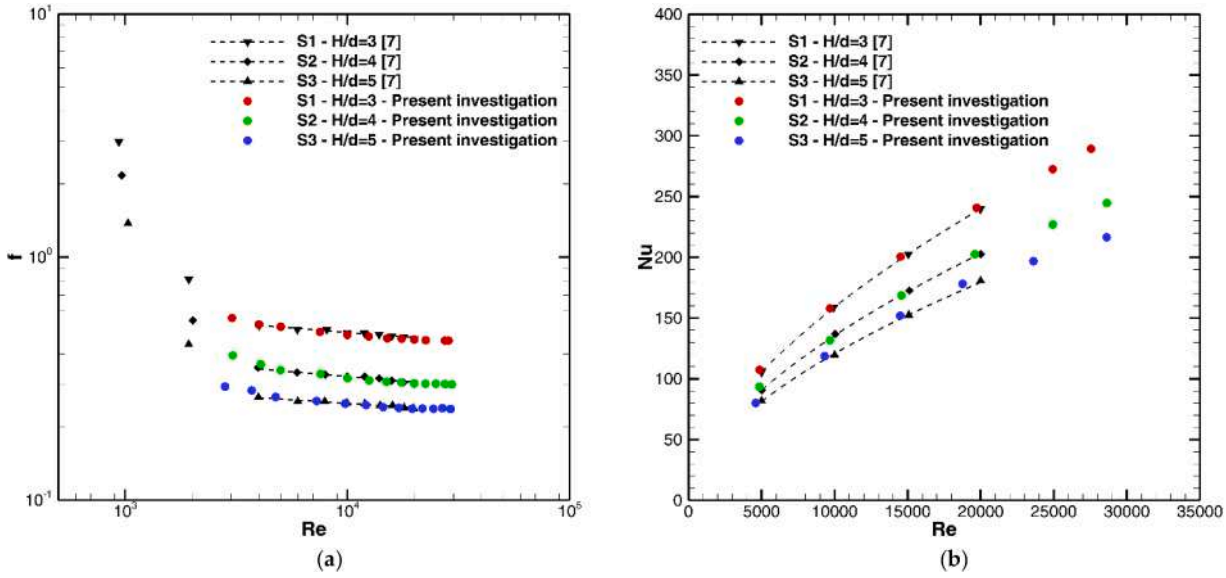

Fig. 17. Aerothermal performances of the heat sinks with circular cross-section: (a) friction factor and (b) Nusselt number.

Thanks to these modified definitions, the final correlations assume the compact and elegant forms given below

$$f = 4.8361\ Re^{-0,0881}\left(\frac{d}{D_{BCC}}\right)^{1,0881} \Leftrightarrow f^* = 4.8361(Re^*)^{-0,0881} \tag{18}$$

$$Nu = 1,7475\ Re^{0,5570}\left(\frac{d}{D_{BCC}}\right)^{0,4430} \Leftrightarrow Nu^* = 1,7475(Re^*)^{0,5570} \tag{19}$$

By so doing, all the experimental data become remarkably superimposed to single lines (see Fig. 18), thus showing the effectiveness of the definitions given above. The average deviation of the experimental points from the best-fit curves are about ±2.8 % and ±4.2 % respectively for Nu^* and f^*. It has to be mentioned that the correlations work for self-similar structures. Therefore, a change of beam angles or cross sections (as examples) will determine performance variations that cannot be taken into account by the present formulation of the correlations' equations.

4.2. Heat sinks with tapered cross-section

In Fig. 19 the results obtained with the BCC structures having a tapered cross section are compared to those having the more classical circular section. In terms of friction factor, it can be observed that samples S4–S6 have comparable values, that are on average 6 % lower than those obtained with the circular sample S2, i.e. the sample with the same blockage effect to the fluid (the frontal dimension d is the same for S2, S4–S6, see Fig. 1(c)). This result indicates that the reduction of form drag of the tapered cross section with respect to the circular one overcomes the augmented skin friction due to the larger wetted surface.

Conversely, the augmented wetted surface has a beneficial effect on the heat transfer: ellipse, drop and cam cross sections perform always better than the circular one with the same frontal dimension (S2) and, in particular, the ellipse shape S4 exhibits superior Nu values that are comparable with those measured with S1. A possible way to evaluate the trade-off between pressure loss increase and heat transfer enhancement due to the adoption of the BCC is to exploit the thermal performance

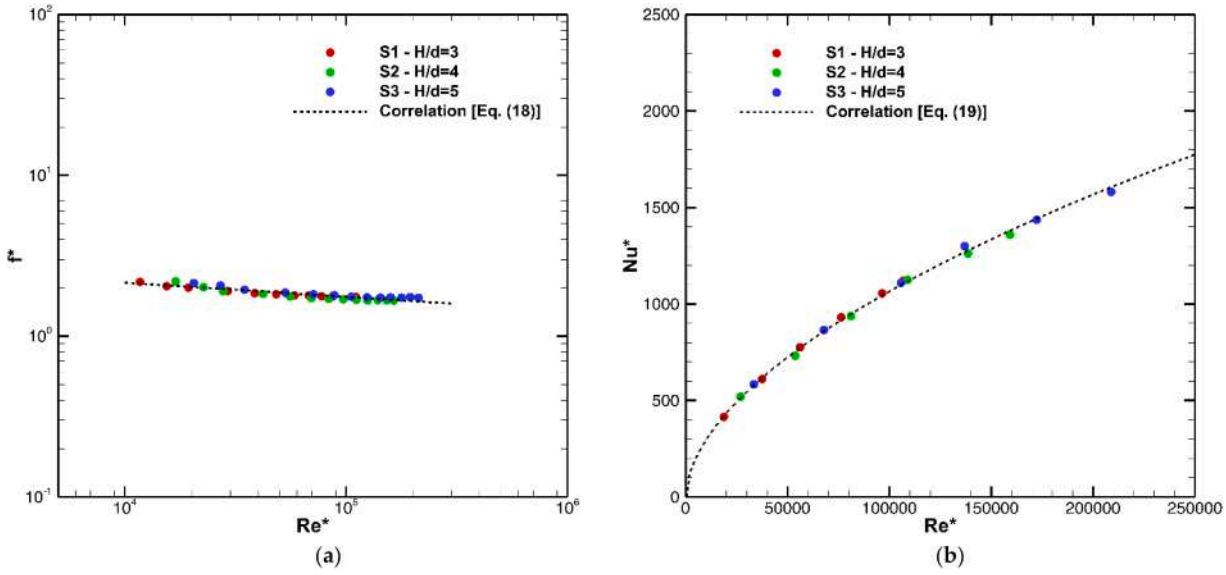

Fig. 18. Correlation to predict the aerothermal performances of the heat sinks with a circular cross-section: (a) modified friction factor and (b) modified Nusselt number as a function of the modified Reynolds number.

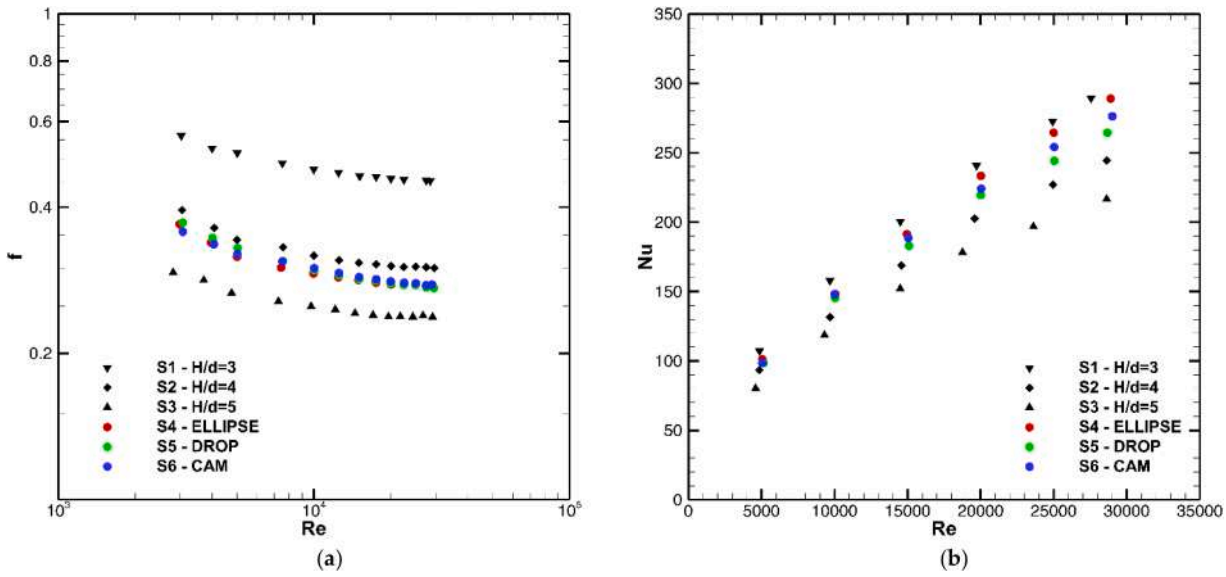

Fig. 19. Comparison of the aero and thermal performances of the heat sinks with circular or tapered cross-section: (a) friction factor and (b) Nusselt number.

factor (TPF) defined as follows:

$$TPF = \frac{Nu/f^{1/3}}{Nu_0/f_0^{1/3}} \tag{20}$$

It compares the thermal efficiency index ($Nu/f^{1/3}$) introduced by [50] with respect to the same parameter computed for the smooth channel case at the same Reynolds number. The values of the thermal efficency for the smooth channel were not derived from the present experiments but were obtained from literature correlations, namely Eq. (14) for the friction factor [48] already used in Section 3.2 (with the same value of $\varepsilon/D_h = 0.006$), and the Gnielinski correlation [51] for the Nusselt number, here reported for sake of completeness.

$$Nu = \frac{(f/8)(Re - 1000)Pr}{1 + 12.7(f/8)^{0.5}(Pr^{2/3} - 1)} \tag{21}$$

The data are reported for Re>5′000, i.e. in the validity range of both Eqs. (21) and (14).

The TPF data reported in Fig. 20 show that the thermal efficiency of the BCC with circular cross section struts are similar for the three values of the diameter considered here, as already reported in [7]. Thanks to the new data it is possible to observe that their TPF drops below the unitary value for Re>20′000. For this reason, they should not be considered good candidates for an efficient heat transfer enhancement. On the other side, the BCC samples with a tapered cross section showed a considerably better behaviour. TPF values of S4 and S6 remained above the critical unitary threshold up to Re=30′000, while TPF of the drop shape S5 fell below unity at Re≈27′500.

With respect to the BCC with circular cross section having the same frontal dimension (S2), the TPF increases on average of about +11 % when adopting the drop shape (S5), +14 % when adopting the cam shape (S6) and +20 % when considering the ellipse shape (S4), which was confirmed as the most performing shape.

As a final analysis, the modified data normalization proposed for the geometries with circular cross sections (Eqs. (15–17)) is applied to the Ellipse, Drop and Cam geometries. The results are shown in Fig. 21. When adopting such normalization for all the geometries, the experimental data do not match the previously found correlations (Eqs. (18) and (19)) with the same degree of accuracy observed in Fig.18. This should be expected, because the variation of the cross section shape was not considered by the present formulations, as already commented.

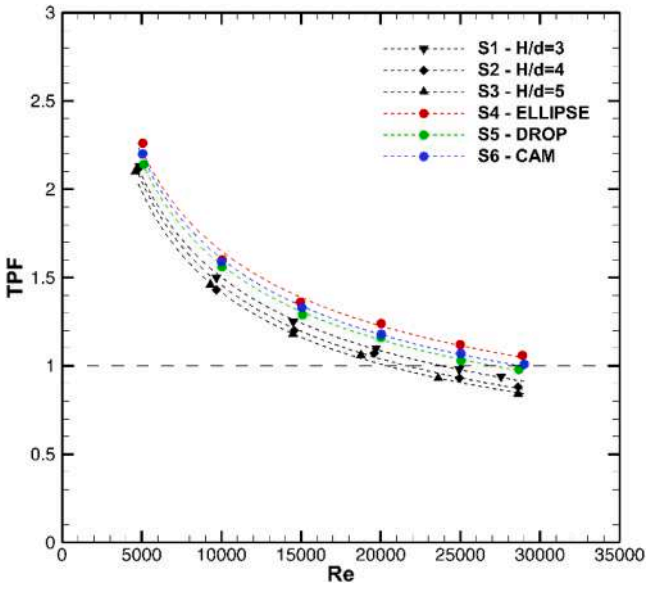

Fig. 20. Thermal performance factor of heat sinks.

5. Conclusions

In this work, the aero and thermal performance of LPBF-produced aluminium heat exchangers featuring a narrow channel filled with staggered BCC structures were experimentally investigated. Building on prior research involving BCC structures with circular cross-section, this work expanded the investigation to higher Reynolds numbers and explored novel cross-section geometries, including elliptical, drop-like, and cam-like shapes.

The preliminary morphological inspections revealed that the geometrical deviation was lower than ±0.25 while the Roughness average R_a of the BCC structures was lower than 6.14 μm. However, some localized defects and low frequency ripples caused by process-induced thermal phenomena and possibly influencing the heat exchanger performance were observed and described.

When considering lattice structures having a circular cross section, the structure with the largest diameter (S1) exhibited the best thermal performance but at the same time a very large pressure drop. The

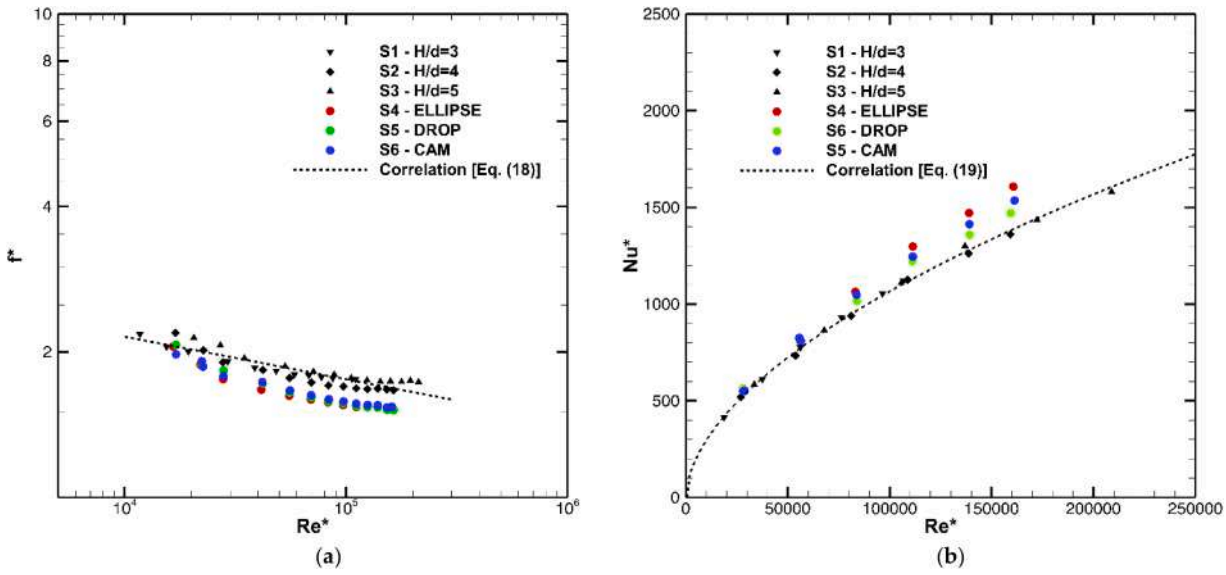

Fig. 21. Comparison of the modified aerothermal performances of the heat sinks: (a) modified friction factor and (b) modified Nusselt number as a function of the modified Reynolds number.

Table 8
Uncertainty value of the experimental parameters.

Measurement	Uncertainty value
T_{IN}, $T_{OUT,C}$	±0.1 K
T_{TC}	±1 K
$\dot{m}$	±1% of the instrument full scale
E	0.01 V
I	0.1 A
Δp	±0.01 mmH_2O
Other pressures	±0.2 mbar
ΔL	±0.5 mm
Other dimensions	±0.05 mm
Aluminum thermal condutivity	±5 %

obtained data confirmed the correlations proposed in [7] predicting the heat transfer and the pressure losses of this type of BCC struts, by also demonstrating their applicability up to Re=30′000.

The tapered cross-sections were capable of reducing pressure losses by an average of 6 % when compared to circular cross-sections of the same size (S2), with no significant differences among the different geometries. Concurrently, drop-like, cam-like, and elliptical cross-sections did significantly increase the Nusselt number of +7 %, +12 %, and +16 % respectively with respect to S2. Interestingly, the thermal performance of the elliptical cross-sections was on average only 3 % lower than the largest circular cross-section (S1), with only half of the pressure losses.

The Thermal Performance Factor for the circular cross-sections dropped below unity at around Re=20′000, while it remained above unity up to Re=30′000 for the tapered cross sections, thus proving their higher efficiency.

CRediT authorship contribution statement

Andrea Lorenzon: Data curation, Investigation, Methodology, Writing – original draft, Writing – review & editing. **Emanuele Vaglio:** Conceptualization, Formal analysis, Investigation, Methodology, Writing – original draft, Writing – review & editing. **Luca Casarsa:** Conceptualization, Data curation, Formal analysis, Funding acquisition, Investigation, Methodology, Project administration, Resources, Supervision, Validation, Writing – original draft, Writing – review & editing. **Giovanni Totis:** Conceptualization, Writing – original draft, Writing – review & editing.

Declaration of competing interest

The authors declare that they have no known competing financial interests or personal relationships that could have appeared to influence the work reported in this paper.

Data availability

Data will be made available on request.

Acknowledgments

The Laboratory for Advanced Mechatronics - LAMA FVG - of the University of Udine is gratefully acknowledged. LAMA FVG is an international research centre for product and process innovation where the three Universities of Friuli Venezia Giulia Region (Italy) synergically cooperate for promoting R&D activities at academic and industrial levels. The Authors would also like to thank Mr. Claudio Giordani (master's degree student) for his enthusiasm and attention to the contribution he made to this work. Emanuele Vaglio is grateful for funding under the REACT EU Italian PON 2014–2020 Program - Action IV.4 - Innovation (DM 1062, 10/08/2021).

Appendix: Uncertainty estimation

The uncertainty about the aero and thermal performances (namely on the Nusselt and Reynolds numbers and on the friction factor) were derived from the method by Kline and McClintock's [52]. This analysis does not apply to the PIV data where a different approach has been used and reported at

the end of this appendix.

The error propagation analysis starts from the uncertainty affecting the single measurements reported in Table 8 and are the same values used in the previous contribution [7] since the test rig and the instrumentations are the same. The value associated to the thermocouples measuring the flow temperature is particularly low because the probes have been calibrated in a thermal bath against the reading from a PT100 1/10 DIN accuracy class.

The Reynolds numbers were evaluated within an uncertainty below 3.8 % for values above 5,000. Larger uncertainties affected the smooth channel case at lower Reynolds numbers (up to 19 % at Re=1′000).

The friction factor data for the heat sinks geometries has an upper bound of about 15 %, however this applies for flow conditions with Reynolds number below 10,000. At higher Reynolds numbers the uncertainty of the friction factor estimate can be considered below 8.5 %. For the smooth channel the friction factor uncertainty was relatively high at Re=1′000 (less or equal to 33 %), but it decreases to less than 15 % at Re=30,000.

The Nusselt number uncertainty was mostly affected by the error associated to the evaluation of the internal surface temperature, while the flow temperature plays a minor role. The maximum uncertainty associated to the Nusselt number was 9.5 %, which was found at low Reynolds numbers, when the thermal input was minimum. At the highest flow regimes (Re=30′000) this value drops down to about 6.2 %. The experimental repeatability was attested within the 8 % based on 6 tests replicated at the extreme flow conditions.

Concerning the PIV flow data, a different approach was used. Since only statistical quantities are reported (and not data from instantaneous flow fields), the error associated to the computations of the statistics from a limited number of uncorrelated samples is considered and it can be computed as follows [53]:

$$err_U = \frac{S[U]}{U} = \frac{Z_c}{\sqrt{N}}\frac{U'}{U}, \quad err_{U'} = \frac{S[U']}{U'} = \frac{Z_c}{\sqrt{2N}} \tag{A1}$$

where U is the generic (averaged) velocity component, err is its relative error, $S[U]$ its standard deviation, U' its fluctuations, Z_c is the confidence coefficient (equal to 1.96 for a 95 % confidence level) and N is the number of uncorrelated samples (in the present case $N = 1000$). Due to the limited number of available samples, the sampling error is assumed as the upper bound error. In the present case, because of the variation of the turbulence activity in the flow (i.e. inside the boundary layer subject of the PIV investigation), the sampling error is a function of the actual position inside the flow. However, the uncertainty in the mean and rms velocities turns out to be less than 2 % and 4.1 %, respectively, over the whole investigated flow regions.

References

[1] U. Sajjad, T. Rehman, M. Ali, C.W. Park, W.M. Yan, Manufacturing and potential applications of lattice structures in thermal systems: a comprehensive review of recent advances, Int. J. Heat Mass Transf. 198 (2022) 123352.

[2] P. Ekade, S. Krishnan, Fluid flow and heat transfer characteristics of octet truss lattice geometry, Int. J. Therm. Sci. 137 (2019) 253–261.

[3] I. Kaur, P. Singh, Flow and thermal transport through unit cell topologies of cubic and octahedron families, Int. J. Heat Mass Transf. 158 (2020) 119784.

[4] C. Moon, H.D. Kim, K.C. Kim, Kelvin-cell-based metal foam heat exchanger with elliptical struts for low energy consumption, Appl. Therm. Eng. 144 (2018) 540–550.

[5] T. Dixit, P. Nithiarasu, S. Kumar, Numerical evaluation of additively manufactured lattice architectures for heat sink applications, Int. J. Therm. Sci. 159 (2021) 106607.

[6] D. Liang, W. Bai, W. Chen, M.K. Chyu, Investigating the effect of element shape of the face-centered cubic lattice structure on the flow and endwall heat transfer characteristics in a rectangular channel, Int. J. Heat Mass Transf. 153 (2020) 119579.

[7] A. Lorenzon, E. Vaglio, L. Casarsa, M. Sortino, Experimental investigation of heat transfer and pressure losses across staggered Body Centered cubic arrays fabricated by Laser Powder Bed Fusion, Appl. Therm. Eng. 227 (2023) 120381.

[8] T. Dixit, E. Al-Hajri, M.C. Paul, P. Nithiarasu, S. Kumar, High performance, microarchitected, compact heat exchanger enabled by 3D printing, Appl. Therm. Eng. 210 (2022) 118339.

[9] Z. Cheng, R. Xu, P.X. Jiang, Morphology, flow and heat transfer in triply periodic minimal surface based porous structures, Int. J. Heat Mass Transf. 170 (2021) 120902.

[10] A. Takezawa, X. Zhang, M. Kitamura, Optimization of an additively manufactured functionally graded lattice structure with liquid cooling considering structural performances, Int. J. Heat Mass Transf. 143 (2019) 118564.

[11] R. Mahshid, H.N. Hansen, K.L. Højbjerre, Strength analysis and modeling of cellular lattice structures manufactured using selective laser melting for tooling applications, Mater. Des. 104 (2016) 276–283.

[12] A.G. Caket, C. Wang, M.A. Nugroho, H. Celik, M. Mobedi, Recent studies on 3D lattice metal frame technique for enhancement of heat transfer: discovering trends and reasons, Renew. Sustain. Energy Rev. 167 (2022) 112697.

[13] C. Brandt, N. Schüler, M. Gaderer, J.M. Kuckelkorn, Development of a thermal oil operated waste heat exchanger within the off-gas of an electric arc furnace at steel mills, Appl. Therm. Eng. 66 (2014) 335–345.

[14] C. Frantz, R. Buck, M. Röger, B. Hoffschmidt, Experimental analysis of forced convective heat transfer of nitrate salt in a circular tube at high Reynolds numbers and temperatures, Int. J. Heat Mass Transf. 201 (2023) 123563.

[15] O.E. Akay, M. Das, Modeling the total heat transfer coefficient of a nuclear research reactor cooling system by different methods, Case Stud. Therm. Eng. 25 (2021) 100914.

[16] F.N. Nourin, R.S. Armano, Review of gas turbine internal cooling improvement technology, J. Energy Resour. Technol. 143 (2021) 080801.

[17] L. Ventola, F. Robotti, M. Dialameh, F. Calignano, D. Manfredi, E. Chiavazzo, P. Asinari, Rough surfaces with enhanced heat transfer for electronics cooling by direct metal laser sintering, Int. J. Heat Mass Transf. 75 (2014) 58–74.

[18] K.N. Son, J.A. Weibel, V. Kumaresan, S.V. Garimella, Design of multifunctional lattice-frame materials for compact heat exchangers, Int. J. Heat Mass Transf. 115 (2017) 619–629.

[19] Y. Zhang, D. Kong, S. Liu, Experimental study of forced convection heat transfer of graded metal honeycomb fabricated by additive manufacturing, Int. Commun. Heat Mass Transf. 98 (2018) 67–73.

[20] D. Shamvedi, O.J. McCarthy, E. O'Donoghue, C. Danilenkoff, P. O'Leary, R. Raghavendra, 3D Metal printed heat sinks with longitudinally varying lattice structure sizes using direct metal laser sintering, Virtual Phys. Prototyp. 13 (2018) 301–310.

[21] K.K. Wong, K.C. Leong, Saturated pool boiling enhancement using porous lattice structures produced by selective laser melting, Int. J. Heat Mass Transf. 121 (2018) 46–63.

[22] A. Takezawa, X. Zhang, M. Kato, M. Kitamura, Method to optimize an additively-manufactured functionally-graded lattice structure for effective liquid cooling, Addit. Manuf. 28 (2019) 285–298.

[23] G. Yang, C. Hou, M. Zhao, W. Mao, Comparison of convective heat transfer for Kagome and tetrahedral truss-cored lattice sandwich panels, Sci. Rep. 9 (2019) 1–13.

[24] J.Y. Ho, K.C. Leong, T.N. Wong, Experimental and numerical investigation of forced convection heat transfer in porous lattice structures produced by selective laser melting, Int. J. Therm. Sci. 137 (2019) 276–287.

[25] C. Hou, G. Yang, X. Wan, J. Chen, Study of thermo-fluidic characteristics for geometric-anisotropy Kagome truss-cored lattice, Chinese J. Aeronaut. 32 (2019) 1635–1645.

[26] A. Chaudhari, P. Ekade, S. Krishnan, Experimental investigation of heat transfer and fluid flow in octet-truss lattice geometry, Int. J. Therm. Sci. 143 (2019) 64–75.

[27] P. Cova, D. Santoro, D. Spaggiari, F. Portesine, F. Vaccaro, N. Delmonte, CFD modeling of additive manufacturing liquid cold plates for more reliable power press-pack assemblies, Microelectron. Reliab. 114 (2020) 113734.

[28] S. Yun, J. Kwon, D. Lee, H.H. Shin, Y. Kim, Heat transfer and stress characteristics of additive manufactured FCCZ lattice channel using thermal fluid-structure interaction model, Int. J. Heat Mass Transf. 149 (2020) 119187.

[29] J.Y. Ho, K.C. Leong, T.N. Wong, Additively-manufactured metallic porous lattice heat exchangers for air-side heat transfer enhancement, Int. J. Heat Mass Transf. 150 (2020) 119262.

[30] S. Yun, D. Lee, D.S. Jang, M. Lee, Y. Kim, Numerical analysis on thermo-fluid-structural performance of graded lattice channels produced by metal additive manufacturing, Appl. Therm. Eng. 193 (2021) 117024.

[31] I. Kaur, P. Singh, Endwall heat transfer characteristics of octahedron family lattice-frame materials, Int. Commun. Heat Mass Transf. 127 (2021) 105522.

[32] R. Tucker, M. Khatamifar, W. Lin, K. McDonald, Experimental investigation of orientation and geometry effect on additive manufactured aluminium LED heat sinks under natural convection, Therm. Sci. Eng. Progr. 23 (2021) 100918.

[33] K. Altaf, A. Tariq, S.W. Ahmad, G. Hussain, T.A.H. Ratlamwala, H.M. Ali, Thermal and hydraulic analysis of slotted plate fins heat sinks using numerical and experimental techniques, Case Stud. Therm. Eng. 35 (2022) 102109.
[34] S. Takarazawa, K. Ushijima, R. Fleischhauer, J. Kato, K. Terada, W.J. Cantwell, M. Kaliske, S. Kagaya, S. Hasumoto, Heat-transfer and pressure drop characteristics of micro-lattice materials fabricated by selective laser metal melting technology, Heat Mass Transf. 58 (2022) 125–141.
[35] L. Xu, H. Chen, L. Xi, Y. Xiong, J. Gao, Y. Li, Flow and heat transfer characteristics of a staggered array of Kagome lattice structures in rectangular channels, Heat Mass Transf. 58 (2022) 41–64.
[36] F. Alawwa, M. Saeed, R. Homsi, H. Zhu, A.S. Berrouk, M. Khalil, G. Xie, Y. Al Wahedi, Thermohydraulic performance comparison of 3D printed circuit heatsinks with conventional integral fin heatsinks, Appl. Therm. Eng. 226 (2023) 120356.
[37] W.J. Luo, P. Vishwakarma, B. Panigrahi, Hydrodynamic influence on thermal management of flexible heatsink devices embedded with out-of-plane intricate microchannel design, Int. Commun.Heat Mass Transf. 144 (2023) 106792.
[38] J. Pearl, J. Paterson, K. Flinders, N. Mantel, J.H. You, Cyclic medium heat flux testing of a WTa lattice structure on the HIVE facility, Fusion Eng. Des. 194 (2023) 113699.
[39] R. Rahmani, J. Karimi, N. Kamboj, R. Kumar, M. Brojan, A. Tchórz, G. Skrabalak, S. I. Lopes, Fabrication of localized diamond-filled copper structures via selective laser melting and spark plasma sintering, Diam. Relat. Mater. 136 (2023) 109916.
[40] D. Kong, E. Jung, Y. Kim, V.V. Manepalli, K.J. Rah, H.S. Kim, Y. Hong, H.G. Choi, D. Agonafer, H. Lee, An additively manufactured manifold-microchannel heat sink for high-heat flux cooling, Int. J. Mech. Sci. 248 (2023) 108228.
[41] S.Y. Lee, K.W. Kim, D.H. Kim, M.S. Yang, J.W. Kim, G. Choi, J.W. Lee, I.S. Park, Optimization study on the uniform temperature of an additively manufactured cooler for a semiconductor heating device, Appl. Therm. Eng. 225 (2023) 120178.
[42] A. Lorenzon, E. Vaglio, L. Casarsa, M. Sortino, G. Totis, G. Saragò, E. Lendormy, J. Raukola, Heat transfer and pressure loss performances for additively manufactured pin fin arrays in annular channels, Appl. Therm. Eng. 202 (2022) 117851.
[43] A. Diani, L. Moro, L. Rossetto, Melting of paraffin waxes embedded in a porous matrix made by additive manufacturing, Appl. Sci. 11 (2021) 5396.
[44] Y.A. Cengel, A.J. Ghajar, Heat Mass Transfer Fundamentals and Applications, 5th ed., McGraw-Hill Professional, 2014.
[45] M. Fernelius, S. Gorrell, Thermocouple Recovery Factor for Temperature Measurements in Turbomachinery Test Facilities, in: Proceedings of the 52nd AIAA Aerospace Sciences Meeting – AIAA Science and Technology Forum and Exposition, 2014, p. 0791.
[46] K. Iwamoto, Y. Suzuki, N. Kasagi, Database of Fully Developed Channel flow, Internal report, University of Tokyo, Japan, 2002. http://www.thtlab.t.u-tokyo.ac.jp/DNS/ILR-0201.pdf.
[47] C.F. Colebrook, C.M. White, Experiments with fluid friction in roughened pipes, Proc. Royal Soc. Lond. Ser. A Math. Phys. Sci. 161 (1937) 367–381.
[48] S.E. Haaland, Simple and explicit formulas for the friction factor in turbulent flow, J. Fluids Eng. 105 (1983) 89–90.
[49] J.E. Hesselgreaves, R. Law, D. Reay, Compact Heat Exchangers Selection, Design and Operation, 2nd ed., Butterworth-Heinemann, 2016.
[50] J. Tian, T. Kim, T.J. Lu, H.P. Hodson, D.T. Queheillalt, D.J. Sypeck, H.N.G. Wadley, The effects of topology upon fluid-flow and heat-transfer within cellular copper structures, Int. J. Heat Mass Transf. 47 (2004) 3171–3186.
[51] V. Gnielinski, New equations for heat mass transfer in turbulent pipe and channel flow, Int. Chem. Eng. 16 (1976) 359–368.
[52] S. Kline, F. McClintock, Describing uncertainties in single-sample Experiments, Mech. Eng. 75 (1953) 3–8.
[53] J.S. Bendat, A.G. Piersol, Random Data Analysis and Measurement Procedures, John Wiley & Sons, 1986.